



HAL
open science

Discontinuity-scale path-following methods for the embedded discontinuity finite element modeling of failure in solids

Giuseppe Rastiello, Francesco Riccardi, Benjamin Richard

► **To cite this version:**

Giuseppe Rastiello, Francesco Riccardi, Benjamin Richard. Discontinuity-scale path-following methods for the embedded discontinuity finite element modeling of failure in solids. *Computer Methods in Applied Mechanics and Engineering*, 2019, 349, pp.431-457. 10.1016/j.cma.2019.02.030 . cea-02074573

HAL Id: cea-02074573

<https://cea.hal.science/cea-02074573>

Submitted on 20 Mar 2019

HAL is a multi-disciplinary open access archive for the deposit and dissemination of scientific research documents, whether they are published or not. The documents may come from teaching and research institutions in France or abroad, or from public or private research centers.

L'archive ouverte pluridisciplinaire **HAL**, est destinée au dépôt et à la diffusion de documents scientifiques de niveau recherche, publiés ou non, émanant des établissements d'enseignement et de recherche français ou étrangers, des laboratoires publics ou privés.

Discontinuity-scale path-following methods for the embedded discontinuity finite element modeling of failure in solids

Giuseppe Rastielo^{a,*}, Francesco Riccardi^{a,1}, Benjamin Richard^{a,2}

^a*DEN - Service d'études mécaniques et thermiques (SEMT), CEA, Université Paris-Saclay, 91191, Gif-sur-Yvette, France*

Abstract

The initiation and propagation of cracks in solids often leads to unstable structural responses characterized by snap-backs. Path-following procedures allow finding a solution to the algebraic system of equations resulting from the numerical formulation of the considered problem. Accordingly, the boundary value problem is supplemented by a novel global unknown, namely, the loading factor, which should comply with a dedicated equation, the so-called path-following constraint equation. In this contribution, path-following methods are discussed within the framework of the Embedded Finite Element Method (E-FEM). Thanks to the enhanced kinematic description provided by the E-FEM, we show that it is possible to formulate constraint equations where the prescribed quantities are directly related to the dissipative process occurring at the strong discontinuity level. After introducing the augmented E-FEM formulation, three discontinuity-scale path-following constraints and their numerical implementation (using an operator-splitting method) are described. Simple quasi-static strain localization problems characterized by unstable structural responses exhibiting multiple snap-backs are numerically simulated. A comparison with several well-known constraint equations (commonly used in non-linear finite element computations) is finally established. This allows for illustrating the main features of the proposed methods as well as their efficiency in controlling highly unstable embedded discontinuity finite element simulations.

Keywords: Path-following methods, Strong discontinuities, Embedded finite element method, Dissipative path-following constraints, Operator-splitting method

DOI: <https://doi.org/10.1016/j.cma.2019.02.030>

1. Introduction

Solids subjected to loading are often characterized by the initiation and propagation of damaged bands and cracks. Under some circumstances (e.g., for quasi-brittle materials [1]), the strain localization process leads to the formation of discontinuity surfaces (from a kinematic viewpoint) on which energy is dissipated. Since elastic unloading occurs around the regions where damage concentrates, an elastic energy release takes place. When the released energy exceeds the dissipative capacity of the structure, snap-backs may come up in the structural response.

The numerical simulation of structural problems dealing with snap-backs is a challenging task, especially in computational solid mechanics. In particular, due to the simultaneous decrease of the force and displacement

*Corresponding author

Email address: giuseppe.rastielo@cea.fr (Giuseppe Rastielo)

¹Present address: LMT, ENS Paris-Saclay, CNRS, Université Paris-Saclay, 94235, Cachan, France

²Present address: IRSN, Structural Performance Modeling and Analysis Laboratory, F-92260, Fontenay-aux-Roses, France

in the global structural response (Fig. 1), conventional force and displacement control methods do not ensure achieving convergence in the post-critical regime (i.e., when such instabilities occur). Once the onset of instabilities is achieved the structural response cannot be controlled, and convergence cannot be reached either.

Path-following methods [2] enable overcoming these issues. In these formulations, the evolution of the external actions is no more assumed as known *a-priori*, but is updated along with the deformation process based on a given criterion. From a mathematical viewpoint, this leads to supplement the equilibrium problem with an additional problem unknown, namely the loading factor, which should comply with a dedicated equation, the so-called path-following constraint equation.

Initially introduced for the simulation of unstable responses associated with geometrical non-linearities [3, 4, 5], the so-called “arc-length methods” were extensively used to deal with structural instabilities. In these formulations, constraint equations are expressed as functions of the norm of the whole degrees of freedom (DOFs) of the problem. As underlined by many authors, however, this choice is not suitable when dealing with material instabilities [6, 2]. Indeed, due to the highly localized nature of the strain localization process in solids, strong non-linearities are associated with a limited number of DOFs. As a consequence, arc-length methods may fail in evaluating the force in the post-peak regime.

Since the pioneering work of [6], many algorithms were proposed in the literature to overcome these limitations. Among them, one should mention path-following constraints on the rate of variation of selected sets of DOFs [6, 7], on strain measures [8, 9, 10] or on variables directly associated with the energy dissipation occurring in the system during damage propagation [11, 12, 13, 14, 15, 16]. Hybrid geometric-dissipative arc-length methods were also proposed (see e.g. [17]) in order to ensure a continuous variation of the nature of the constraint along with the deformation process.

These techniques were successfully applied to non-linear finite element simulations where material non-linearities were represented using continuum damage mechanics models [13, 18], phase-field formulations [14], Thick Level-Set (TLS) damage models [19]. Path-following methods were also used in strong discontinuity simulations, where cracks were modeled using zero-thickness interface finite elements [20, 13, 17], in the eXtended Finite Element Method (X-FEM) [21] and in the Embedded Finite Element Method (E-FEM) [22, 23, 24]. This latter framework is considered in this work.

According to this approach [25, 26, 27, 28, 29, 30], the enhanced displacement field representing the displacement jump associated with the crack is embedded at the elemental level. Thanks to a static condensation procedure, enhanced displacements are computed by solving elemental traction continuity conditions (in weak form), without changing the total number of degrees of freedom of the global equilibrium problem. The resulting numerical implementation is therefore less intrusive than the X-FEM method [31, 32, 33, 34], while preserving an enhanced kinematics description.

Since constraint equations are generally functions of continuous variables (e.g. total displacement field, total strain field), their integration in standard E-FEM implementations can be achieved in a slightly intrusive way. These methods may, however, fail in some circumstances, in particular when dissipative and elastic equilibrium solutions should be distinguished [13].

Given the enhanced kinematics description provided by strong discontinuity formulations, one could therefore think of deriving constraint equations by prescribing the evolution of variables associated with the non-linear (dissipative) response of the elemental discontinuities directly. In the case of the E-FEM, the integration of this kind of constraint equations in the iterative procedure for solving the non-linear mechanical problem has not been formalized yet. Presenting such a kind of path-following methods, describing their numerical implementation and showing some representative results are the main objectives of the present work.

The article is structured as follows. After presenting briefly a finite element formulation with embedded strong discontinuities, a reformulation of path-following methods in this framework is proposed. Then, three constraint equations are formulated to drive the mechanical response at the strong discontinuity level. Finally, simple numerical test cases involving unstable structural responses characterized by one or more

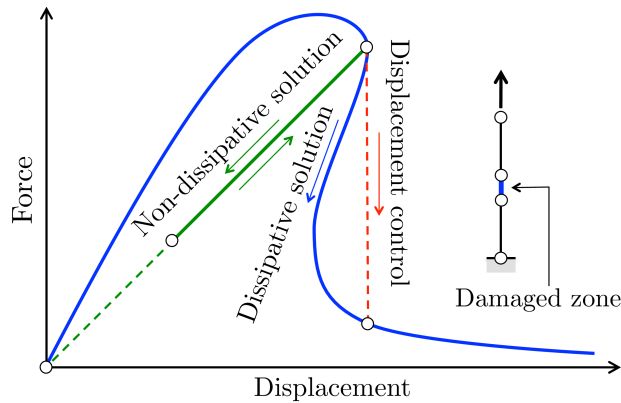


Figure 1: Dissipative and non-dissipative solutions for a simple unidimensional damage mechanics localization problem exhibiting an unstable structural response characterized by a snap-back.

snap-backs are presented. Assuming that the bulk always remains in elastic regime and that dissipation occurs at the embedded discontinuity level only, the proposed control constraints are discussed and compared. For this purpose, several well-known path-following constraints classically adopted in continuum finite element simulations are also considered. Some conclusions and perspectives close the paper.

2. Finite elements with embedded discontinuities

This section presents the E-FEM formulation that is considered in this work. After introducing the enhanced strong discontinuity kinematics, the Boundary Value Problem (BVP) is illustrated. The resulting equilibrium equations are finally discretized in space based on the “Statically and Kinematically Optimal Nonsymmetric” (SKON) formulation first proposed in [35, 26] and better studied in [36].

2.1. Strong discontinuity kinematics

Consider a n_{dim} -dimensional domain $\Omega \subset \mathbb{R}^{n_{dim}}$ crossed by a discontinuity line/surface $\Gamma \subset \mathbb{R}^{n_{dim}}$ dividing the body into two non-overlapping parts Ω^- and Ω^+ (Fig. 2). The displacement field $\mathbf{u} = \mathbf{u}(\mathbf{x}, t) : \Omega \times [0, T] \rightarrow \mathbb{R}^{n_{dim}}$ at time $t \in [0, T]$ can be written as:

$$\mathbf{u} = \bar{\mathbf{u}} + \mathcal{H}_\Gamma[\llbracket \mathbf{u} \rrbracket] \quad (1)$$

where $\bar{\mathbf{u}} = \bar{\mathbf{u}}(\mathbf{x}, t) : \Omega \times [0, T] \rightarrow \mathbb{R}^{n_{dim}}$ is the continuous part of the displacement field, $\llbracket \mathbf{u} \rrbracket = \llbracket \mathbf{u} \rrbracket(\mathbf{x}, t) : \Omega \times [0, T] \rightarrow \mathbb{R}^{n_{dim}}$ denotes the displacement jump function and $\mathcal{H}_\Gamma = \mathcal{H}_\Gamma(\mathbf{x})$ is the Heaviside unit step function centered on Γ (\mathcal{H}_Γ is equal to unity on Ω^+ and is null otherwise).

The infinitesimal strain field $\boldsymbol{\epsilon} = \boldsymbol{\epsilon}(\mathbf{x}, t) : \Omega \times [0, T] \rightarrow \mathbb{R}^{n_{dim} \times n_{dim}}$ kinematically compatible with the discontinuous displacement field (1) reads:

$$\boldsymbol{\epsilon} = \nabla^s \mathbf{u} = \nabla^s \bar{\mathbf{u}} + \mathcal{H}_\Gamma \nabla^s \llbracket \mathbf{u} \rrbracket + \delta_\Gamma (\llbracket \mathbf{u} \rrbracket \otimes \mathbf{n})^s \quad (2)$$

where “ ∇ ” is the gradient operator, upper-script s denotes the symmetric part operator, $\mathbf{n} = \mathbf{n}(\mathbf{x})$ is the normal to the discontinuity line/surface, symbol “ \otimes ” is the dyadic product between second order tensors and $\delta_\Gamma = \delta_\Gamma(\mathbf{x})$ is the Dirac’s delta distribution function on Γ (δ_Γ is equal to $+\infty$ on Γ and is null otherwise).

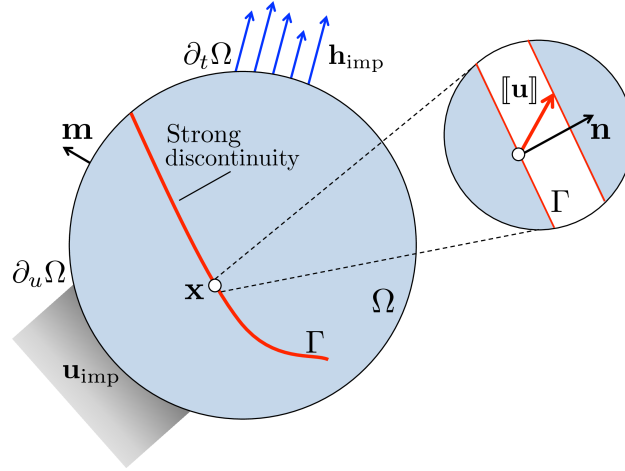


Figure 2: Domain Ω crossed by a discontinuity line Γ and definition of the quantities of interest

2.2. Discrete strong discontinuity formulation

Two contributions to the strain field (2) can be distinguished. The first one ($\nabla^s \bar{\mathbf{u}} + \mathcal{H}_\Gamma \nabla^s \llbracket \mathbf{u} \rrbracket$) is bounded whereas the term arising from the displacement jump ($\delta_\Gamma (\llbracket \mathbf{u} \rrbracket \otimes \mathbf{n})^s$) is singular in the distributional sense. Such a singularity brings inconsistencies into the continuum constitutive equations. To overcome this issue, a so-called Discrete Strong Discontinuity Approach (DSDA) is considered [37, 38]. Accordingly, we assume that a continuum stress - strain law holds in the bulk material, whereas a discrete constitutive relationship links the traction vector (\mathbf{t}) between the crack surfaces to $\llbracket \mathbf{u} \rrbracket$ on Γ . A traction continuity condition finally ensures fulfilling the equilibrium condition across the cracked region.

2.3. Boundary value problem in a strong discontinuity setting

Strong form. Infinitesimal strain and quasi-static loading conditions are considered. In the absence of body forces, solving the BVP consists in finding – at any time t – an admissible displacement field such that:

$$\operatorname{div} \boldsymbol{\sigma} = \mathbf{0}, \quad \text{on } \Omega \quad (3)$$

$$\boldsymbol{\sigma} = \mathcal{F}(\boldsymbol{\epsilon}), \quad \text{on } \Omega \quad (4)$$

$$\boldsymbol{\epsilon} = \nabla^s \mathbf{u}, \quad \text{on } \Omega \quad (5)$$

$$\mathbf{u} = \mathbf{u}_{\text{imp}}, \quad \text{on } \partial_u \Omega \quad (6)$$

$$\boldsymbol{\sigma} \mathbf{m} = \mathbf{h}_{\text{imp}}, \quad \text{on } \partial_t \Omega \quad (7)$$

$$\mathbf{t} = \mathcal{G}(\llbracket \mathbf{u} \rrbracket) \quad \text{on } \Gamma \quad (8)$$

$$\llbracket \boldsymbol{\sigma} \rrbracket \mathbf{n} = \mathbf{0}, \quad \text{on } \Gamma \quad (9)$$

$$\boldsymbol{\sigma} \mathbf{n} - \mathbf{t} = \mathbf{0}, \quad \text{on } \Gamma \quad (10)$$

where “div” denotes the divergence operator, $\boldsymbol{\sigma} = \boldsymbol{\sigma}(\mathbf{x}, t) : \Omega \times [0, T] \rightarrow \mathbb{R}^{n_{\text{dim}} \times n_{\text{dim}}}$ is the Cauchy stress tensor, \mathcal{F} is a continuum constitutive relationship between $\boldsymbol{\sigma}$ and $\boldsymbol{\epsilon}$, $\partial \Omega \subset \mathbb{R}^{n_{\text{dim}}}$ denotes the boundary of the domain, $\mathbf{m} = \mathbf{m}(\mathbf{x})$ is the outward normal to $\partial \Omega$, \mathbf{u}_{imp} is the imposed displacements vector on $\partial_u \Omega \subset \partial \Omega$, \mathbf{h}_{imp} is the traction vector prescribed on $\partial_t \Omega \subset \partial \Omega$. Furthermore, $\llbracket \boldsymbol{\sigma} \rrbracket = \llbracket \boldsymbol{\sigma} \rrbracket(\mathbf{x}, t)$ is the stress jump across the discontinuity and \mathcal{G} is the constitutive law describing the response of the discontinuity (i.e., the traction-separation law). The split of the boundary of the domain is such that $\partial \Omega = \overline{\partial_u \Omega} \cup \overline{\partial_t \Omega}$ and $\partial_u \Omega \cap \partial_t \Omega = \emptyset$, where the superposed line denotes a closure.

Weak form. The weak form of the BVP is derived by applying the general Hu-Washizu variational principle [39, 40]. For this purpose, three independent fields (\mathbf{u} , $\boldsymbol{\epsilon}$, $\boldsymbol{\sigma}$) and the corresponding admissible variations

$(\mathbf{u}^*, \boldsymbol{\epsilon}^*, \boldsymbol{\sigma}^*)$ are considered. After application of the Green theorem to the term containing \mathbf{u}^* , and provided the independence of $(\mathbf{u}^*, \boldsymbol{\epsilon}^*, \boldsymbol{\sigma}^*)$, the following variational equality is obtained:

$$\forall (\mathbf{u}^*, \boldsymbol{\epsilon}^*, \boldsymbol{\sigma}^*) \in (\mathcal{U}, \mathcal{E}, \mathcal{S})$$

$$\int_{\Omega} \boldsymbol{\epsilon}^* : \tilde{\boldsymbol{\sigma}}(\boldsymbol{\epsilon}) \, dv + \int_{\Omega} \boldsymbol{\sigma}^* : (\nabla^s \mathbf{u} - \boldsymbol{\epsilon}) \, dv + \int_{\Omega} \boldsymbol{\sigma} : (\nabla^s \mathbf{u}^* - \boldsymbol{\epsilon}^*) \, dv - \int_{\partial_t \Omega} \mathbf{u}^* \cdot \mathbf{h}_{\text{imp}} \, ds = 0 \quad (11)$$

where “:” denotes the standard double contraction between symmetric second order tensors, “.” is the Euclidean inner product between vectors in $\mathbb{R}^{n_{dim}}$, $\tilde{\boldsymbol{\sigma}}(\boldsymbol{\epsilon})$ satisfies the constitutive law (4), $\mathcal{U} = \{\mathbf{u}^* \mid \mathbf{u}^* \in H^1(\Omega), \mathbf{u}^* = 0 \text{ on } \partial_u \Omega\}$, $\mathcal{E} = \{\boldsymbol{\epsilon}^* \mid \boldsymbol{\epsilon}^* \in L^2(\Omega)\}$ and $\mathcal{S} = \{\boldsymbol{\sigma}^* \mid \boldsymbol{\sigma}^* \in L^2(\Omega)\}$.

2.4. Embedded discontinuity finite element problem

The domain Ω is discretized through a finite element mesh Ω^h comprising n_{el} elements Ω_e and n_{nt} nodes. The discretization is such that $\Omega^h = \bigcup_{e=1}^{n_{el}} \Omega_e$ and $\bigcap_{e=1}^{n_{el}} \Omega_e = \emptyset$. Inside $\Omega_e \subset \Omega^h$, the following nodal interpolations are considered:

$$\mathbf{u} = \mathbf{N}\mathbf{d} + \mathbf{N}_c \mathbf{d}_c \quad \boldsymbol{\epsilon} = \mathbf{B}\mathbf{d} + \mathbf{G}\mathbf{e} \quad \boldsymbol{\sigma} = \mathbf{S}\mathbf{s} \quad (12)$$

where \mathbf{d} is the nodal displacements vector, \mathbf{d}_c is the elemental enhanced displacements vector, \mathbf{e} denotes the enhanced strains vector and \mathbf{s} is the elemental stress vector. Furthermore, $\mathbf{N} = \mathbf{N}(\mathbf{x})$ is the displacement interpolation (elemental shape functions) matrix, $\mathbf{N}_c = \mathbf{N}_c(\mathbf{x})$ denotes the enhanced displacements interpolation operator, $\mathbf{B} = \mathbf{B}(\mathbf{x}) = \mathbf{L}\mathbf{N}$ is the total strains interpolation matrix (\mathbf{L} computes ∇^s), $\mathbf{G} = \mathbf{G}(\mathbf{x})$ is the interpolation operator of the enhanced strains associated with \mathbf{e} . Similar interpolations are adopted for virtual fields, with the exception of $\boldsymbol{\epsilon}^*$. For the sake of generality, this latter is approximated as $\boldsymbol{\epsilon}^* = \mathbf{B}\mathbf{d}^* + \mathbf{G}^* \mathbf{e}^*$, with $\mathbf{G}^{*\top}$ denoting the interpolation operator for the enhanced virtual strains \mathbf{e}^* .

Given the independence of variations $(\mathbf{u}^*, \boldsymbol{\epsilon}^*, \boldsymbol{\sigma}^*)$ and assuming $\mathbf{d}_c = \mathbf{e}$, replacing approximations introduced above into the variational identity (11), after some mathematical manipulations yields:

$$\mathbf{f}_{\text{int}}(\mathbf{d}, \mathbf{e}) - \mathbf{f}_{\text{ext}} = \mathbf{A} \int_{e=1}^{n_{el}} \int_{\Omega_e} \mathbf{B}^{\top} \boldsymbol{\sigma}(\mathbf{d}, \mathbf{e}) \, dv - \mathbf{A} \int_{e=1}^{n_{el}} \int_{\partial_t \Omega_e} \mathbf{N}^{\top} \mathbf{h}_{\text{imp}} \, ds = \mathbf{0} \quad (13)$$

$$\int_{\Omega_e} \mathbf{G}^* \boldsymbol{\sigma}(\mathbf{d}, \mathbf{e}) \, dv = \mathbf{0} \quad \forall \Omega_e \in \Omega_{\text{loc}}^h \quad (14)$$

where $\boldsymbol{\sigma}(\mathbf{d}, \mathbf{e}) = \mathcal{F}(\mathbf{B}\mathbf{d} + \mathbf{G}\mathbf{e})$, symbol \mathbf{A} denotes the assembly operator, and Ω_{loc}^h is the set of all localized (cracked) elements:

$$\Omega_{\text{loc}}^h \subset \Omega^h := \{\Omega_e \in \Omega^h : \Omega_e \cap \Gamma \neq \emptyset\} \quad (15)$$

In the following, we will consider that each finite element can be crossed by a single strong discontinuity line/surface (Γ_e). Moreover, linear Constant Strain Triangular (CST) elements will be used for the sake of simplicity. In that case, the numerical integration of elemental operators is performed through a single point located at the gravity center of Ω_e and the enhanced displacements are directly evaluated at the same location. Slightly more complex formulations are obtained for other elements, e.g. quadrilateral elements with piece-wise linear jump interpolations [41, 42].

2.5. Statically and Kinematically Optimal Nonsymmetric (SKON) formulation

Different choices are possible concerning the nodal interpolation of the enhanced displacement and strain fields (i.e., concerning the definition of operators \mathbf{G} and \mathbf{G}^*). A comparative study of existing methods was proposed by [36]. More recently, [24] performed a detailed numerical comparison of embedded strong discontinuity methods based upon different error norms and evaluated their variational consistency.

According to the classification introduced by [36], three families of formulations should be distinguished: “Statically Optimal Symmetric” (SOS), “Kinematically Optimal Symmetric” (KOS) and SKON formulations. In particular, for the SOS formulation, \mathbf{G} is a matrix with zero mean over the element and $\mathbf{G}^* = \mathbf{G}^{\top}$.

For the KOS formulation, $\mathbf{G} = \mathbf{B}_c = \mathbf{L}\mathbf{N}_c$ and $\mathbf{G}^* = \mathbf{G}^\top = \mathbf{B}_c^\top$. Finally, for the SKON formulation, $\mathbf{G} = \mathbf{B}_c$ and matrix \mathbf{G}^* is chosen to ensure that the element passes the patch-test (zero mean condition).

This latter approximation is considered in this work. Accordingly, operator \mathbf{G}^* is chosen as follows:

$$\mathbf{G}^* = \left(\delta_\Gamma - \frac{\text{meas}(\Gamma_e)}{\text{meas}(\Omega_e)} \right) \mathbf{P}^\top \quad (16)$$

where “ $\text{meas}(\Omega_e)$ ” denotes the elemental area/volume, “ $\text{meas}(\Gamma_e)$ ” is a measure of the discontinuity line/surface inside Ω_e , and matrix \mathbf{P} contains the components of \mathbf{n} . Finally, interpolation operators \mathbf{N}_c and \mathbf{G} are defined as:

$$\mathbf{N}_c = \mathcal{H}_\Gamma - \sum_{n_a \in \Omega_e^+} \mathbf{N}_a \quad \mathbf{G} = \mathbf{B}_c = \mathbf{L}\mathbf{N}_c = \delta_\Gamma \mathbf{P} - \sum_{a \in \Omega_e^+} \mathbf{B}_a \quad (17)$$

where \mathbf{N}_a is the elementary restriction of \mathbf{N} to nodes $n_a \in \Omega_e^+$ and $\mathbf{B}_a = \mathbf{L}\mathbf{N}_a$. Notice that, in previous definitions, we supposed that the elemental discontinuity splits Ω_e into two sub-elements Ω_e^+ and Ω_e^- such that vector \mathbf{n} is inward Ω_e^+ .

By substituting definition (16) into (14), and exploiting the properties of the Dirac’s delta function, one obtains the following local/discontinuity-scale momentum balance equation:

$$\frac{1}{\text{meas}(\Omega_e)} \int_{\Omega_e} \mathbf{P}^\top \boldsymbol{\sigma}(\mathbf{d}, \mathbf{e}) \, dv - \underbrace{\frac{1}{\text{meas}(\Gamma_e)} \int_{\Gamma_e} \mathbf{t}(\mathbf{e}) \, ds}_{:=\bar{\mathbf{t}}(\mathbf{e})} = \mathbf{0} \quad (18)$$

The latter equation represents the weak averaged traction continuity condition (10) over the finite element crossed by the discontinuity. For CST elements, equation (18) can be simplified as follows:

$$\mathbf{P}^\top \boldsymbol{\sigma}(\mathbf{d}, \mathbf{e}) - \mathbf{t}(\mathbf{e}) = \mathbf{0} \quad (19)$$

3. Path-following algorithms in the Embedded Finite Element Method

The formulation of path-following algorithms in the E-FEM context is addressed in this section. After deriving the linearized finite element formulation of the augmented equilibrium problem, we show that path-following procedures can be naturally formulated in this framework. Provided the static condensation of the enhanced fields at the elemental level, we demonstrate that decomposing the nodal displacement field in an additive way – as it is classically done in path-following methods – leads to a similar split of the enhanced displacement field. Thanks to the enriched kinematics description proper to the E-FEM, it is therefore possible to prescribe the evolution of both global DOFs and local variables associated with the dissipative response of the strong discontinuity.

3.1. Augmented embedded discontinuity finite element problem

In order to introduce path-following constraints into the numerical formulation, the external force vector is rewritten as [3]:

$$\mathbf{f}_{\text{ext}} = \mathbf{f}_{\text{ext},0} + \mathbf{f}_{\text{ext},\lambda} = \mathbf{f}_{\text{ext},0} + \lambda \hat{\mathbf{f}} \quad (20)$$

where $\mathbf{f}_{\text{ext},0}$ is known (user-defined) external forces contribution, $\mathbf{f}_{\text{ext},\lambda}$ an unknown (controlled indirectly) external forces contribution, $\hat{\mathbf{f}}$ is a normalized vector defining the direction of $\mathbf{f}_{\text{ext},\lambda}$ and $\lambda \in \mathbb{R}$ is a variable loading parameter. In a similar manner, the Dirichlet boundary conditions read:

$$\mathbf{d}_{\text{imp}} = \mathbf{d}_{\text{imp},0} + \mathbf{d}_{\text{imp},\lambda} = \mathbf{d}_{\text{imp},0} + \lambda \hat{\mathbf{d}} \quad (21)$$

where $\mathbf{d}_{\text{imp},0}$ is a known contribution and vector $\hat{\mathbf{d}}$ provides the direction of the unknown (indirectly controlled) displacement $\mathbf{d}_{\text{imp},\lambda}$. The loading parameter λ is an additional problem unknown which shall comply with a path-following constraint equation.

The augmented E-FEM problem to solve finally consists in finding a triplet $(\mathbf{d}, \mathbf{e}, \lambda)$ such that:

$$\mathbf{r}(\mathbf{d}, \mathbf{e}, \lambda) = \mathbf{f}_{\text{int}}(\mathbf{d}, \mathbf{e}) - \mathbf{f}_{\text{ext},0} - \lambda \hat{\mathbf{f}} = \mathbf{0} \quad (22)$$

$$\mathbf{r}_{\text{loc}}^e(\mathbf{d}, \mathbf{e}) = \mathbf{P}^\top \boldsymbol{\sigma}(\mathbf{d}, \mathbf{e}) - \mathbf{t}(\mathbf{e}) = \mathbf{0} \quad \forall \Omega_e \in \Omega_{\text{loc}}^h \quad (23)$$

$$P(\mathbf{d}, \mathbf{e}, \lambda; \tau) = 0 \quad (24)$$

with the boundary condition (21). In previous equations, $\mathbf{r}(\mathbf{d}, \mathbf{e}, \lambda)$ is the global residual (global out-of-balance force) vector, $\mathbf{r}_{\text{loc}}^e(\mathbf{d}, \mathbf{e})$ are the local residuals (local out-of-balance forces) associated with the elemental traction continuity conditions, equation (24) defines the path-following constraint and τ is the user-defined path-step length. This latter can be regarded as a pseudo-time parameter.

3.2. Linearized problem

Previous equations are discretized in pseudo-time according to an ordered sequence of steps $[t_0, t_1, \dots, T]$, such that $t_{n+1} > t_n$ for all $n \in \mathbb{N}$. Given the solution $\mathbf{a}_n = \{\mathbf{d}_n, \mathbf{e}_n, \lambda_n\}$ at time t_n , one looks for the solution variation $\Delta \mathbf{a} = \{\Delta \mathbf{d}, \Delta \mathbf{e}, \Delta \lambda\}$ in the interval $[t_n, t_{n+1}]$ such that $\mathbf{a} = \mathbf{a}_n + \Delta \mathbf{a}$ at time t_{n+1} . Given the non-linear nature of constitutive equations usually adopted in computations, the incremental problem is solved by means of an iterative procedure. The total solution increment at global iteration $k+1$ is thus written as $\Delta \mathbf{a}^{k+1} = \mathbf{a}^{k+1} - \mathbf{a}_n = \Delta \mathbf{a}^k + \delta \mathbf{a}^{k+1}$, where $\delta \mathbf{a}^{k+1} = \{\delta \mathbf{d}^{k+1}, \delta \mathbf{e}^{k+1}, \delta \lambda^{k+1}\}$ is the solution variation between two successive iterations³.

3.2.1. Global and local equilibrium equations

By performing a truncated Taylor expansion of equilibrium equations (22) and (23) around the solution $(\mathbf{d}^k, \mathbf{e}^k, \lambda^k)$, one obtains the following linearized equations:

$$-\mathbf{r}^k = \mathbf{K}_{bb}^k \delta \mathbf{d}^{k+1} + \mathbf{K}_{bg}^k \delta \mathbf{e}^{k+1} - \hat{\mathbf{f}} \delta \lambda^{k+1} \quad (25)$$

$$-\mathbf{r}_{\text{loc}}^{e,k} = \mathbf{K}_{gb}^{e,k} \delta \mathbf{d}^{k+1} + \mathbf{K}_{gg}^{e,k} \delta \mathbf{e}^{k+1} \quad \forall \Omega_e \in \Omega_{\text{loc}}^h \quad (26)$$

where $\mathbf{r}^k = \mathbf{r}(\mathbf{d}^k, \mathbf{e}^k, \lambda^k)$ and $\mathbf{r}_{\text{loc}}^{e,k} = \mathbf{r}_{\text{loc}}^e(\mathbf{d}^k, \mathbf{e}^k)$. Furthermore, the stiffness operators \mathbf{K}_{bb}^k , \mathbf{K}_{bg}^k , $\mathbf{K}_{gb}^{e,k}$ and $\mathbf{K}_{gg}^{e,k}$ read:

$$\mathbf{K}_{bb}^k = \mathbf{A} \mathbf{K}_{bb}^{e,k} = \mathbf{A} \int_{\Omega_e} \mathbf{B}^\top \mathbf{D}^k \mathbf{B} \, dv \quad (27)$$

$$\mathbf{K}_{bg}^k = \mathbf{A} \mathbf{K}_{bg}^{e,k} = \mathbf{A} \int_{\Omega_e} \mathbf{B}^\top \mathbf{D}^k \mathbf{G} \, dv \quad (28)$$

$$\mathbf{K}_{gb}^{e,k} = \int_{\Omega_e} \mathbf{G}^* \mathbf{D}^k \mathbf{B} \, dv \quad (29)$$

$$\mathbf{K}_{gg}^{e,k} = \int_{\Omega_e} \mathbf{G}^* \mathbf{D}^k \mathbf{G} \, dv \quad (30)$$

with $\mathbf{D}^k = (\partial_e \boldsymbol{\sigma})^k$ denoting the stiffness tensor of the bulk material at iteration k ($\partial_\bullet = \partial/\partial\bullet$ is the partial derivation with respect to variable \bullet). It should be noticed that any other stiffness tensor could have been considered as soon as it leads to a symmetric, positive-definite stiffness matrix.

³In previous equations, down-script $n+1$ was omitted for the sake of compactness. The same nomenclature will be used in the following. As a consequence of this, any quantity without down-script should be intended as referring to pseudo-time t_{n+1} .

Decomposition of total and enhanced displacements. According to the arguments introduced above, the loading factor can be written as $\lambda^{k+1} = \lambda^k + \delta\lambda^{k+1}$. Introducing this decomposition into a standard incremental finite element formulation leads to write $\delta\mathbf{d}^{k+1} = \delta\lambda^{k+1}\delta\mathbf{d}_I^{k+1} + \delta\mathbf{d}_{II}^{k+1}$, where $\delta\mathbf{d}_I^{k+1}$ and $\delta\mathbf{d}_{II}^{k+1}$ are solved from two independent systems of equations. In the following we show that such decomposition is still valid in a E-FEM framework. Furthermore, a similar decomposition is obtained for $\delta\mathbf{e}^{k+1}$.

In order to derive this formulation, let us consider the case of one or more finite elements experiencing strain localization. Solving equation (26) with respect to $\delta\mathbf{e}^{k+1}$ yields:

$$\delta\mathbf{e}^{k+1} = -(\mathbf{K}_{gg}^{e,k})^{-1}\mathbf{K}_{gb}^{e,k}\delta\mathbf{d}^{k+1} - (\mathbf{K}_{gg}^{e,k})^{-1}\mathbf{r}_{loc}^{e,k} \quad \forall \Omega_e \in \Omega_{loc}^h \quad (31)$$

By substituting this expression into (25) and solving with respect to $\delta\mathbf{d}^{k+1}$ one obtains:

$$\tilde{\mathbf{K}}_{bb}^k \delta\mathbf{d}^{k+1} = \hat{\mathbf{f}} \delta\lambda^{k+1} - \mathbf{r}^k + \mathbf{A}_{e=1}^{n_{el}} [\varphi^e \mathbf{K}_{bg}^{e,k} (\mathbf{K}_{gg}^{e,k})^{-1} \mathbf{r}_{loc}^{e,k}] \quad (32)$$

with $\tilde{\mathbf{K}}_{bb}^k$ denoting the enhanced (condensed) stiffness operator of the bulk:

$$\tilde{\mathbf{K}}_{bb}^k = \mathbf{A}_{e=1}^{n_{el}} [\mathbf{K}_{bb}^{e,k} - \varphi^e \mathbf{K}_{bg}^{e,k} (\mathbf{K}_{gg}^{e,k})^{-1} \mathbf{K}_{gb}^{e,k}] = \mathbf{K}_{bb}^k - \mathbf{A}_{e=1}^{n_{el}} [\varphi^e \mathbf{K}_{bg}^{e,k} (\mathbf{K}_{gg}^{e,k})^{-1} \mathbf{K}_{gb}^{e,k}] \quad (33)$$

and where $\varphi^e = \varphi^e(\Omega_e)$ is a binary function indicating if Ω_e is localized or not. It is defined as:

$$\varphi^e = \begin{cases} 1 & \text{if } \Omega_e \in \Omega_{loc}^h \\ 0 & \text{otherwise} \end{cases} \quad (34)$$

The nodal displacement increment can therefore be expressed as:

$$\delta\mathbf{d}^{k+1} = \delta\lambda^{k+1}\delta\mathbf{d}_I^{k+1} + \delta\mathbf{d}_{II}^{k+1} \quad (35)$$

where $\delta\mathbf{d}_I^{k+1}$ and $\delta\mathbf{d}_{II}^{k+1}$ are solved from:

$$\tilde{\mathbf{K}}_{bb}^k \delta\mathbf{d}_I^{k+1} = \hat{\mathbf{f}} \quad \text{and} \quad \tilde{\mathbf{K}}_{bb}^k \delta\mathbf{d}_{II}^{k+1} = -\mathbf{r}^k + \mathbf{A}_{e=1}^{n_{el}} [\varphi^e \mathbf{K}_{bg}^{e,k} (\mathbf{K}_{gg}^{e,k})^{-1} \mathbf{r}_{loc}^{e,k}] \quad (36)$$

Note that decomposition (35) is usual in path-following methods. Furthermore, a standard continuum mechanics formulation [2] is recovered when $\Omega_{loc}^h = \emptyset$. In that case, contributions associated with the enhanced displacement field vanish, and nodal displacement variations are calculated by solving: $\mathbf{K}_{bb}^k \delta\mathbf{d}_I^{k+1} = \hat{\mathbf{f}}$ and $\mathbf{K}_{bb}^k \delta\mathbf{d}_{II}^{k+1} = -\mathbf{r}^k$.

By replacing relationship (35) into (31):

$$\delta\mathbf{e}^{k+1} = -(\mathbf{K}_{gg}^{e,k})^{-1}\mathbf{K}_{gb}^{e,k}(\delta\lambda^{k+1}\delta\mathbf{d}_I^{k+1} + \delta\mathbf{d}_{II}^{k+1}) - (\mathbf{K}_{gg}^{e,k})^{-1}\mathbf{r}_{loc}^{e,k} \quad (37)$$

and collecting terms multiplied by $\delta\lambda^{k+1}$, it is easy to verify that a similar additive decomposition holds for the enhanced displacement field too. In particular, one obtains:

$$\delta\mathbf{e}^{k+1} = \delta\lambda^{k+1}\delta\mathbf{e}_I^{k+1} + \delta\mathbf{e}_{II}^{k+1} \quad \forall \Omega_e \in \Omega_{loc}^h \quad (38)$$

where contributions $\delta\mathbf{e}_I^{k+1}$ and $\delta\mathbf{e}_{II}^{k+1}$ are solved from:

$$\mathbf{K}_{gg}^{e,k} \delta\mathbf{e}_I^{k+1} = -\mathbf{K}_{gb}^{e,k} \delta\mathbf{d}_I^{k+1} \quad \text{and} \quad \mathbf{K}_{gg}^{e,k} \delta\mathbf{e}_{II}^{k+1} = -\mathbf{K}_{gb}^{e,k} \delta\mathbf{d}_{II}^{k+1} - \mathbf{r}_{loc}^{e,k} \quad (39)$$

3.2.2. Path-following constraint equations

In addition to the above given equations of equilibrium, the constraint equation should also be fulfilled. Regarding its linearization, however, two main situations should be distinguished depending on the differentiability properties of function $P = P(\mathbf{d}, \mathbf{e}, \lambda; \tau)$.

Case 1. When P is differentiable with respect to $(\mathbf{d}, \mathbf{e}, \lambda)$, equation (24) can be linearized:

$$P^{k+1} = P^k + (\partial_{\mathbf{d}}P)^k \delta \mathbf{d}^{k+1} + (\partial_{\mathbf{e}}P)^k \delta \mathbf{e}^{k+1} + (\partial_{\lambda}P)^k \delta \lambda^{k+1} = 0 \quad (40)$$

and an explicit formula for the loading factor variation derived. Substituting decompositions (35) and (38) inside (40), and solving for $\delta \lambda^{k+1}$ yields:

$$\delta \lambda^{k+1} = - \frac{P^k + (\partial_{\mathbf{d}}P)^k \delta \mathbf{d}_{\text{II}}^{k+1} + (\partial_{\mathbf{e}}P)^k \delta \mathbf{e}_{\text{II}}^{k+1}}{(\partial_{\mathbf{d}}P)^k \delta \mathbf{d}_{\text{I}}^{k+1} + (\partial_{\mathbf{e}}P)^k \delta \mathbf{e}_{\text{I}}^{k+1} + (\partial_{\lambda}P)^k} \quad (41)$$

Once again, when $\Omega_{\text{loc}}^h = \emptyset$, terms associated with the enhanced displacements disappear from (41) and a standard formulation [2] is recovered.

Differentiability can be guaranteed, for instance, when path-following constraints are written in terms of sets of global DOFs fixed *a priori* [6, 7]. Widely used in continuum mechanics computations, these control techniques may reveal very useful for numerically reproducing experimental loading conditions [43, 44]. However, under complex conditions involving unstable responses characterized by multiple snap-backs (e.g. in the presence of multiple propagating strong discontinuities), these formulations lose much of their robustness and may fail due to the difficulty of choosing a set of controlled DOFs ensuring that a solution to the underlying incremental problem exists.

Case 2. More robust constraint equations can be obtained by allowing λ to evolve based on a condition defined by maximizing a quantity of interest $z = z(\mathbf{x})$ over Ω . For instance, by requiring that the maximum variation of z (e.g. a strain measure, a local energy dissipation) is equal to $\Delta \tau$ somewhere in the structure. Denoting with $\alpha \in \Omega^h$ a part (or a numerical entity) of the discretized domain (e.g. a finite element, an integration point, an elemental discontinuity), the constraint equation may be written as:

$$P^{k+1} = \max_{\alpha \in \Omega^h} (\Delta z_{\alpha}^{k+1}) - \Delta \tau = \max_{\alpha \in \Omega^h} (\Delta z_{\alpha}^k + \delta z_{\alpha}^{k+1}) - \Delta \tau = 0 \quad (42)$$

where $\delta z_{\alpha}^{k+1} = \delta z_{\alpha}^{k+1}(\delta \mathbf{d}_{\text{I}}^{k+1}, \delta \mathbf{d}_{\text{II}}^{k+1}, \delta \mathbf{e}_{\text{I}}^{k+1}, \delta \mathbf{e}_{\text{II}}^{k+1}, \delta \lambda^{k+1})$ through decompositions (35) and (38). By doing so, entities α potentially experiencing the higher increments of the controlled quantity can be searched automatically and are updated along with the solving process.

The main drawback of this approach is that function (42) is no more differentiable, and a direct estimation of $\delta \lambda^{k+1}$ is no more possible. However, the computation can be performed through an iterative procedure, e.g. a nested interval algorithm [13].

3.3. Operator-splitting solution method

Thanks to the static condensation of the enhanced DOFs at the elemental level, equilibrium equations (36) and (39) can be solved sequentially through an “operator splitting method” [45] (such strategy is often called staggered static condensation [46, 47]). In this way, the size of the global problem to solve is unchanged compared to a standard FEM formulation, and the numerical implementation can be achieved in slightly intrusive way. The whole solution procedure can be summarized according to three main steps as follows. Given the solution $(\mathbf{d}^k, \mathbf{e}^k, \lambda^k)$ at iteration k :

- (i) The nodal displacement increments $(\delta \mathbf{d}_{\text{I}}^{k+1}, \delta \mathbf{d}_{\text{II}}^{k+1})$ are first computed from (36) while keeping the enhanced displacements fixed;
- (ii) The enhanced displacement corrections $(\delta \mathbf{e}_{\text{I}}^{k+1}, \delta \mathbf{e}_{\text{II}}^{k+1})$ are then calculated by solving traction continuity conditions (39) localized element by localized element, while keeping nodal displacements constant. Since non-linear traction-separation laws are typically adopted in computations, local incremental iterative procedures are used to solve traction continuity conditions at the elemental level.
- (iii) Finally, the loading factor increment $\delta \lambda^{k+1}$ is estimated. This calculation is performed after computing the displacement increments. As a consequence, it can be implemented in a dedicated subroutine and easily adapted to deal with different path-following constraint equations.

3.4. Classification of path-following constraint equations

Several constraint equations can be defined based on the displacement decompositions derived above. In the following, they are classified according to three main families depending on the scale (or algorithmic level) corresponding to the controlled variables.

Global-Scale (GS) constraints are written in terms of large-scale/global quantities (e.g. total displacements, total strains). These control methods are classically used in non-linear FEM simulations. Since nodal displacements account indirectly for the strong discontinuities embedded into finite elements, most of these formulations (e.g. [6, 8, 9, 10]) may be used in E-FEM computations without major modifications.

In this work, however, attention is focused on Discontinuity-Scale (DS) constraints. With this term, we refer to constraint equations where the prescribed quantities are relative to the response of the discontinuity itself (e.g. enhanced displacements, internal variables of the traction-separation law):

$$P^{k+1} = P^{k+1}(\mathbf{e}^k, \lambda^k, \delta \mathbf{e}_I^{k+1}, \delta \mathbf{e}_{II}^{k+1}, \delta \lambda^{k+1}; \Delta \tau) = 0 \quad (43)$$

In this way, one can imagine to drive the propagation of a crack based on the dissipation occurring on the crack tip or inside a fracture/damaging process zone.

Multi-Scale (MS) constraints may also be obtained by combining large- and discontinuity-scale quantities. They could be useful for controlling, for instance, numerical simulations where a transition from damage to fracture is represented by coupling continuum and strong discontinuity models [48]. Their formulation is not investigated further in this work.

4. Discontinuity-Scale path-following constraints

Drawing from methods previously proposed in continuum mechanics contexts (e.g. [13, 19]), three DS path-following constraints are obtained. They are based upon prescribing: (i) the maximum value of the elastic predictor of the yield (damage) criterion function driving the dissipative response of the discontinuity; (ii) the maximum rate of variation of the internal variables of the traction-separation law; (iii) a scalar measure of the enhanced displacement increment.

4.1. Dissipative model

We assume that dissipation occurs on Γ only, while the response of the bulk always remains linear elastic. At the elemental level, the traction-separation law (8) is formulated according to a rate-independent constitutive model with a single internal variable κ_α . Its evolution satisfies the Kuhn-Tucker and consistency conditions:

$$f_\alpha \leq 0 \quad \dot{\kappa}_\alpha \geq 0 \quad \dot{\kappa}_\alpha f_\alpha = 0 \quad \dot{\kappa}_\alpha \dot{f}_\alpha = 0 \quad \forall \alpha \in \Omega_{loc}^h \quad (44)$$

where $f_\alpha = f_\alpha(Y_\alpha, \mathbf{e}_\alpha, \kappa_\alpha)$ is a damage (plastic) criterion function and $Y_\alpha = Y_\alpha(\mathbf{e}_\alpha, \kappa_\alpha)$ is the thermodynamic force associated with κ_α . In the following we will always refer to f_α as the damage criterion function for the sake of homogeneity with test cases illustrated in the next section. Similar considerations hold, however, for plasticity models.

4.2. Constraint on the Maximal Elastic Predictor (DS-CMEP) of the damage criterion function

Initially proposed for rate-independent continuum models [13], a path-following Constraint on the Maximal Elastic Predictor (CMEP) of the damage criterion function (i.e., the value of function f_α when considering an incrementally elastic response) is well suited to capture localized phenomena resulting from strain localization. Furthermore, it allows to distinguish between elastic unloading and dissipative equilibrium solutions. As shown by the cited authors, a positive value of the elastic predictor is associated with a dissipative branch of the equilibrium path. For more details concerning the properties of the CMEP method, the interested reader can refer to [13].

4.2.1. Constraint equation

The path-following CMEP can be adapted easily to problems involving embedded strong discontinuities to obtain the DS-CMEP. In that context, one looks for $\Delta\lambda^{k+1} = \Delta\lambda^k + \delta\lambda^{k+1}$ such that the elastic predictor ($f_\alpha^{\text{elas},k+1}$) of the damage function is equal to $\Delta\tau > 0$ on at least one localized element (and is lower elsewhere). The constraint equation thus reads:

$$P^{k+1} = \max_{\alpha \in \Omega_{\text{loc}}^h} (f_\alpha^{\text{elas},k+1}(\delta\lambda^{k+1})) - \Delta\tau = 0 \quad (45)$$

where:

$$f_\alpha^{\text{elas}}(\delta\lambda^{k+1}) = f(Y_\alpha(\mathbf{e}_\alpha^{k+1}(\delta\lambda^{k+1}), \kappa_{\alpha,n}), \mathbf{e}_\alpha^{k+1}(\delta\lambda^{k+1}), \kappa_{\alpha,n}) \quad \alpha \in \Omega_{\text{loc}}^h \quad (46)$$

with $\kappa_{\alpha,n}$ denoting the internal variable at time t_n and:

$$\mathbf{e}_\alpha^{k+1}(\delta\lambda^{k+1}) = \mathbf{e}_{\alpha,n} + \Delta\mathbf{e}_\alpha^k + \delta\lambda^{k+1}\delta\mathbf{e}_{\alpha,\text{I}}^{k+1} + \delta\mathbf{e}_{\alpha,\text{II}}^{k+1} \quad \alpha \in \Omega_{\text{loc}}^h \quad (47)$$

Notice that, due to the use of an operator splitting method, the only unknown in (46) is $\delta\lambda^{k+1}$. As a consequence, one can write $f_\alpha^{\text{elas}}(\delta\lambda^{k+1}; \lambda^k, \mathbf{e}^k, \delta\mathbf{e}_\text{I}^{k+1}, \delta\mathbf{e}_\text{II}^{k+1})$ or, in a more concise form, $f_\alpha^{\text{elas}}(\delta\lambda^{k+1})$. The same nomenclature will be used in the following.

4.2.2. First loading factor increment

Since solving equation (45) requires that $\Omega_{\text{loc}}^h \neq \emptyset$, this control method cannot be used as long as the deformation process is in elastic regime. A first initialization phase is thus needed. It may consist in computing the loading factor λ_1 (at time $t_1 > t_0$) such that at least one element satisfies the localization condition.

A simple choice to identify the onset of localization consists in using a Rankine's criterion [49, 29, 50]. Accordingly, one computes λ_1 such that the maximum elastic principal stress ($\sigma_{\text{prin}}^{\text{max}} = \sigma_{\text{prin}}^{\text{max}}(\lambda_1)$) equals the tensile strength of the material (σ_t) somewhere in the bulk. Alternatively, one could have considered, for instance, a criterion based on the loss of ellipticity of the governing equations [51, 28].

4.2.3. Loading factor variation $\delta\lambda$

Since f_α is commonly chosen to be a convex function of \mathbf{e}_α , f_α^{elas} is also convex. Furthermore, given the convexity of the “max” function, the path-following constraint (45) preserves the same convexity property. As a consequence, it may admit up to two distinct real or complex (inadmissible) roots. Their direct determination however is often impossible, because function f_α^{elas} is generally non-linear and the “max” operator represents a further source of non-linearity. As mentioned in previous sections, a possible solution strategy may consist in using a “nested interval algorithm”. According to this method, the computation of $\delta\lambda^{k+1}$ is performed in three phases as follows:

- (i) *Initialization.* One initializes the space of admissible solutions as $L_{\delta\lambda} := (-\infty, +\infty)$ and starts looping over $\alpha \in \Omega_{\text{loc}}^h$;
- (ii) *Computation.* For each $\alpha \in \Omega_{\text{loc}}^h$, a loading factor $\delta\lambda_\alpha^{k+1}$ is computed by assuming that (45) is locally satisfied:

$$P_\alpha^{k+1} = f_\alpha^{\text{elas}}(\delta\lambda_\alpha^{k+1}) - \Delta\tau = 0 \quad (48)$$

When closed-form solutions to (48) are not available, iterative root-finding algorithms may be adopted. For this purpose, function f_α^{elas} is approximated as:

$$f_\alpha^{\text{elas}}(\delta\lambda_\alpha) = f_\alpha^{\text{elas}}(\delta\lambda^{\text{ref}}) + \partial_{\delta\lambda} f_\alpha^{\text{elas}}(\delta\lambda^{\text{ref}}) (\delta\lambda_\alpha - \delta\lambda^{\text{ref}}) \quad (49)$$

where upper-script “ref” denotes the reference state for the linearization. The simplest choice consists in using an explicit solution procedure to avoid further local sub-iterations. In that case, $\delta\lambda^{\text{ref}} = 0$ (i.e., $\lambda^{\text{ref}} = \lambda^k$) and $\delta\lambda_\alpha^{k+1}$ can be calculated from:

$$a_{\alpha,0} + \delta\lambda_\alpha^{k+1} a_{\alpha,1} - \Delta\tau = 0 \quad (50)$$

where:

$$a_{\alpha,0} = f_{\alpha}^{\text{elas}}(0) \quad a_{\alpha,1} = \partial_{\delta\lambda} f_{\alpha}^{\text{elas}}(0) \quad (51)$$

with $f_{\alpha}^{\text{elas}}(0) = f(Y_{\alpha}(\mathbf{e}_{\alpha}^{k+1}(0), \kappa_{\alpha,n}), \mathbf{e}_{\alpha}^{k+1}(0), \kappa_{\alpha,n})$ and $\mathbf{e}_{\alpha}^{k+1}(0) = \mathbf{e}_{\alpha,n} + \Delta\mathbf{e}_{\alpha}^k + \delta\mathbf{e}_{\alpha,\text{II}}^{k+1}$.

The interval $L_{\delta\lambda}$ is then updated based on the solution just calculated and the sign of $a_{\alpha,1}$ (to check if the linearization is performed on the ascending or descending branch of the function f_{α}^{elas}):

$$L_{\delta\lambda} := L_{\delta\lambda} \cap \begin{cases} (-\infty, \delta\lambda_{\alpha}^{k+1}] & \text{if } a_{\alpha,1} > 0 \\ [\delta\lambda_{\alpha}^{k+1}, +\infty) & \text{otherwise} \end{cases} \quad (52)$$

If $L_{\delta\lambda} = \emptyset$, no solutions exist. In that case, one should reduce $\Delta\tau$ and restart the iteration process from a known equilibrium condition.

- (iii) *Selection.* If at the end of the procedure $L_{\delta\lambda} \neq \emptyset$, a single value $\delta\lambda^{k+1} \in L_{\delta\lambda}$ is selected based on a user-defined criterion. A possible choice consists in minimizing the global residual [52, 13]:

$$\delta\lambda^{k+1} = \arg \min_{\delta\lambda_{\star}^{k+1} \in L_{\delta\lambda}} ((\mathbf{r}^k)^{\top} \mathbf{r}^{k+1}) \quad (53)$$

where $\mathbf{r}^k = \mathbf{r}^k(\mathbf{d}^k, \mathbf{e}^k, \lambda^k)$ and $\mathbf{r}^{k+1} = \mathbf{r}^{k+1}(\dots, \lambda^k + \delta\lambda_{\star}^{k+1})$. According to [13], such a criterion is stabilizing regarding the convergence of the Newton–Raphson algorithm. A comparative study between different convergence criteria was performed by [21] in the X-FEM context.

4.3. Constraint on the Internal Variables Increment (DS-CIVI)

Based on the linearization of the damage criterion function, it is possible to formulate different dissipative path-following constraints. To illustrate this case, we consider a simple traction–separation law and derive a constraint equation based on controlling the rate of variation ($\Delta\kappa_{\alpha}$) of the internal variable. The loading–unloading conditions discretized in time are now written as:

$$f_{\alpha} \leq 0, \quad \Delta\kappa_{\alpha} \geq 0, \quad f_{\alpha} \Delta\kappa_{\alpha} = 0 \quad (54)$$

where, in a continuum damage mechanics context, κ_{α} may be an equivalent measure of the displacement jump (i.e., of vector \mathbf{e}_{α}) across the discontinuity line/surface. These developments were motivated by the recent implementation by [19] of the TLS damage model by [53]. In the cited work, a linearized damage criterion was used to drive the strain localization process by imposing the maximum rate of variation of the level-set function controlling damage evolution.

4.3.1. Constraint equation

The constraint equation is written requiring that $\Delta\kappa_{\alpha}^{k+1}$ reaches the maximum value $\Delta\tau > 0$ on one localized element and is lower elsewhere:

$$P^{k+1} = \max_{\alpha \in \Omega_{\text{loc}}^h} (\Delta\kappa_{\alpha}^{k+1}(\delta\lambda^{k+1})) - \Delta\tau = 0 \quad (55)$$

4.3.2. Loading factor variation $\delta\lambda$

The procedure for computing $\delta\lambda^{k+1}$ is the same as with the DS-CMEP method. In that case, a $\delta\lambda_{\alpha}^{k+1}$ value should be computed for each elemental discontinuity by solving:

$$P_{\alpha}^{k+1} = \Delta\kappa_{\alpha}^{k+1}(\delta\lambda_{\alpha}^{k+1}) - \Delta\tau = 0 \quad (56)$$

Such problem can be, however, restated in a different way. Indeed, since $\Delta\tau > 0$, fulfilling conditions (54) implies that $f_{\alpha}(\mathbf{e}_{\alpha}^{k+1}, \kappa_{\alpha}^{k+1}) = 0$ for any dissipative process such that $\Delta\kappa_{\alpha}^{k+1} = \Delta\tau$. As a consequence, increments $\delta\lambda_{\alpha}^{k+1}$ can be equivalently computed from:

$$P_{\alpha}^{k+1} = f_{\alpha}(\delta\lambda_{\alpha}^{k+1}) = f_{\alpha}(\mathbf{e}_{\alpha}^{k+1}(\delta\lambda_{\alpha}^{k+1}), \kappa_{\alpha}^{k+1}) = 0 \quad (57)$$

with the constraint:

$$\kappa_\alpha^{k+1} = \kappa_\alpha^k + \delta\kappa_\alpha^{k+1} = \kappa_\alpha^k + \Delta\tau - \Delta\kappa_\alpha^k \quad (58)$$

Once again, since the damage criterion function is non-linear, equation (57) should be solved iteratively. Performing a truncated Taylor expansion of f_α around $(\delta\lambda^{\text{ref}}, \delta\kappa^{\text{ref}})$, and enforcing the incremental constraint $\delta\kappa_\alpha = \Delta\tau - \Delta\kappa_\alpha^{\text{ref}}$, one obtains:

$$f_\alpha(\delta\lambda_\alpha) = f_\alpha(\delta\lambda^{\text{ref}}, \delta\kappa^{\text{ref}}) + \partial_{\delta\lambda} f(\delta\lambda^{\text{ref}}, \delta\kappa^{\text{ref}}) (\delta\lambda_\alpha - \delta\lambda^{\text{ref}}) + \partial_{\delta\kappa} f(\delta\lambda^{\text{ref}}, \delta\kappa^{\text{ref}}) (\Delta\tau - \Delta\kappa_\alpha^{\text{ref}} - \delta\kappa^{\text{ref}}) = 0 \quad (59)$$

Using an explicit solution procedure ($\delta\lambda^{\text{ref}} = 0$, $\delta\kappa^{\text{ref}} = 0$, $\Delta\kappa^{\text{ref}} = \Delta\kappa_\alpha^k$), for the sake of comparison with the DS-CMEP method, yields the following linearized equation to solve at each iteration:

$$a_{\alpha,0} + \delta\lambda_\alpha^{k+1} a_{\alpha,1} - \Delta\tau = 0 \quad (60)$$

where:

$$a_{\alpha,0} = \Delta\kappa_\alpha^k - \frac{f_\alpha(0,0)}{\partial_{\delta\kappa} f_\alpha(0,0)} \quad a_{\alpha,1} = -\frac{\partial_{\delta\lambda} f_\alpha(0,0)}{\partial_{\delta\kappa} f_\alpha(0,0)} \quad (61)$$

It should be notice that, since κ_α is updated throughout convergence iterations, function (59) no more corresponds to the linearized elastic predictor of the damage criterion.

4.4. Constraint on the Enhanced Displacement Increment (DS-CEDI)

Since a derivation of functions f_α and f_α^{elas} with respect to some variables is needed, the implementation of the DS-CMEP and DS-CIVI methods depend on the chosen model (i.e., slight modifications are needed for each model used). An alternative and physically consistent choice, that can be made to avoid case-by-case changes to the numerical formulation, may consist in controlling the simulation through a scalar measure of $\Delta\mathbf{e}_\alpha^{k+1}$ (i.e., the displacement jump variation). In that case, the constraint equation can be written as:

$$P^{k+1} = \max_{\alpha \in \Omega_{\text{loc}}^h} (\mathbf{c}_\alpha^\top \Delta\mathbf{e}_\alpha^{k+1}) - \Delta\tau = 0 \quad (62)$$

where $\Delta\tau > 0$, $\mathbf{c}_\alpha = \mathbf{e}_{\alpha,n} / \|\mathbf{e}_{\alpha,n}\|$ is the direction of vector \mathbf{e}_α at time t_n and:

$$\Delta\mathbf{e}_\alpha^{k+1}(\delta\lambda^{k+1}) = \Delta\mathbf{e}_\alpha^k + \delta\lambda^{k+1} \delta\mathbf{e}_{\alpha,\text{I}}^{k+1} + \delta\mathbf{e}_{\alpha,\text{II}}^{k+1} \quad (63)$$

Equation (62) is again solved through a “nested interval procedure”. The equation to solve localized element by localized element reads:

$$P_\alpha^{k+1} = \mathbf{c}_\alpha^\top \Delta\mathbf{e}_\alpha^{k+1} - \Delta\tau = \mathbf{c}_\alpha^\top (\Delta\mathbf{e}_\alpha^k + \delta\lambda_\alpha^{k+1} \delta\mathbf{e}_{\alpha,\text{I}}^{k+1} + \delta\mathbf{e}_{\alpha,\text{II}}^{k+1}) - \Delta\tau = 0 \quad (64)$$

or, in a more concise form:

$$a_{\alpha,0} + \delta\lambda_\alpha^{k+1} a_{\alpha,1} - \Delta\tau = 0 \quad (65)$$

with:

$$a_{\alpha,0} = \mathbf{c}_\alpha^\top (\Delta\mathbf{e}_\alpha^k + \delta\mathbf{e}_{\alpha,\text{II}}^{k+1}) \quad a_{\alpha,1} = \mathbf{c}_\alpha^\top \delta\mathbf{e}_{\alpha,\text{I}}^{k+1} \quad (66)$$

5. Numerical test cases

Path-following methods developed in the previous sections are studied through one- and two-dimensional quasi-brittle fracture simulations involving unstable structural responses. Although attention is focused on DS methods, two standard GS formulations are also considered for the sake of comparison. They consist in imposing the increment of the linear combination of selected global DOFs (GS-CNDI, Control by Nodal Displacement Increment [6]) and the maximal strain variation over the domain (GS-CMSI, Control by Maximal Strain Increment [8, 9, 10]). Numerical developments were performed using the “CastLab” toolbox [54].

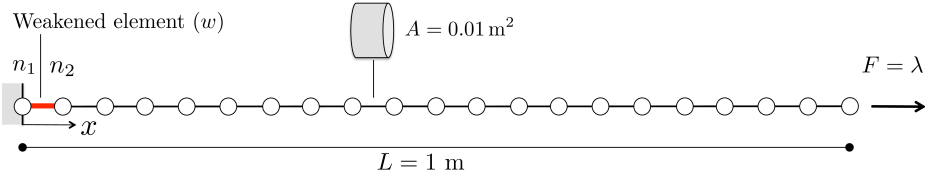


Figure 3: Bar under tension — Geometry, finite element discretization, boundary conditions and quantities of interest

5.1. Constitutive laws

A linear elastic stress-strain constitutive relationship is assumed inside the bulk. The onset of localization is identified based on a Rankine's criterion. For the strong discontinuity, a cohesive traction-separation law is formulated according to a Continuum Damage model with a single scalar variable $D_\alpha \in [0, 1)$. In the local reference system of the elemental discontinuity, the traction force normal to the discontinuity ($t_\alpha = \mathbf{n}_\alpha^\top \mathbf{t}_\alpha$) reads:

$$t_\alpha = t_\alpha(e_\alpha, D_\alpha) = (1 - D_\alpha)K e_\alpha \quad (67)$$

where $e_\alpha = \mathbf{n}_\alpha^\top \mathbf{e}_\alpha$ is the normal displacement jump to Γ_e and K is the initial stiffness of the discontinuity. Its value is defined according to a penalty formulation as $K = \sigma_t / \kappa_{\alpha,0}$, with $\kappa_{\alpha,0} \approx 0$ denoting the normal displacement jump at damage initiation.

The damage criterion function is written in the enhanced displacements space as:

$$f_\alpha = f_\alpha(e_\alpha, \kappa_\alpha) = e_\alpha - \kappa_\alpha \leq 0 \quad (68)$$

where the internal variable κ_α starts at $\kappa_{\alpha,0}$ and is updated as the historical maximum of e_α .

The damage variable rises from zero (not localized element) to unity (fully developed crack) according to the exponential evolution law:

$$D_\alpha = r(\kappa_\alpha) = 1 - \frac{\kappa_0}{\kappa_\alpha} \exp\left(-\frac{\sigma_t}{G_f} \kappa_\alpha\right) \quad (69)$$

where G_f is the fracture energy.

This model was chosen for the sake of simplicity. More advanced constitutive laws, accounting for complex physical mechanisms, can be found in the literature [49, 55, 56, 57]. They can be used in conjunction with path-following methods without significant modifications.

5.2. One-dimensional test case: bar under tension

A one-dimensional body, $L = 1$ m in length and $A = 0.01$ m² in constant transversal cross-section, is submitted to tensile loading (Fig. 3). An indirectly controlled external force ($f_{\text{ext}} = f_{\text{ext},\lambda} = \lambda$) is applied at $x = L$, whereas the displacement is blocked at $x = 0$. The computational domain is discretized through $n_{el} = 20$ linear Bar finite elements. Mechanical parameters are assigned as follows: $E = 30$ GPa (Young's modulus of the bulk), $\sigma_t = 2.8$ MPa and $G_f = 100$ N/m. Strain localization is forced to occur on the element comprised between nodes n_1 and n_2 , the weakened element (denoted with letter w). In this way, the set Ω_{loc}^h contains the weakened element only, the maximum operator can be removed from constraint equations and a first validation of the numerical implementation can be obtained.

5.2.1. Path-following constraint equations

DS-CMEP and DS-CEDI. Given the considered geometrical/loading conditions and damage criterion function (68), function $f_w^{\text{elas}} = e_w^{k+1}(\delta\lambda^{k+1}) - e_{w,n}$ coincides with the total enhanced displacement variation of the weakened element. The DS-CMEP and DS-CEDI constraints thus coincide:

$$P^{k+1} = \Delta e_w^{k+1}(\delta\lambda^{k+1}) - \Delta\tau = \Delta e_w^k + \delta\lambda^{k+1}\delta e_{w,I}^{k+1} + \delta e_{w,II}^{k+1} - \Delta\tau = 0 \quad (70)$$

The loading increment correction can be computed explicitly as:

$$\delta\lambda^{k+1} = \delta\lambda_w^{k+1} = \frac{\Delta\tau - a_{w,0}}{a_{w,1}} \quad (71)$$

where:⁴

$$a_{w,0} = \Delta e_w^k + \delta e_{w,\text{II}}^{k+1} \quad a_{w,1} = \delta e_{w,\text{I}}^{k+1} \quad (72)$$

As mentioned before, solving (70) implies that the weakened element is localized. For that reason, the first loading factor λ_1 (at time $t_1 > t_0 = 0$) is computed from the Rankine's initiation criterion. This yields: $\lambda_1 = \Delta\lambda_1 = \sigma_t A > 0$.

DS-CIVI. When used to control the evolution of κ_w , the DS-CIVI method is very similar to the DS-CMEP. For that reason, it is here adapted to drive the growth of the damage variable D_w . This can be obtained by linearizing the damage criterion function (68) around $\delta\lambda^{\text{ref}}$ and δD^{ref} (instead of $\delta\kappa^{\text{ref}}$), and enforcing the constraint $\delta D_w = \Delta\tau - \Delta D_w^{\text{ref}}$. Employing an explicit solution method for the sake of comparison with the previous case, $\delta\lambda^{k+1}$ can be obtained from equation (71) with:

$$a_{w,0} = \Delta D_w^k - \frac{f_w(0,0)}{\partial_{\delta D} f_w(0,0)} \quad a_{w,1} = -\frac{\partial_{\delta\lambda} f_w(0,0)}{\partial_{\delta D} f_w(0,0)} \quad (73)$$

where $\partial_{\delta D} f_w = (\partial_{\delta\kappa} f_w)(\partial_{\delta D} \kappa_w)$ and $\partial_{\delta D} \kappa_w = \partial_{\delta D}(r^{-1}(D))$.

GS-CNDI. In addition to these discontinuity-scale constraints, a well-known global-scale indirect control method is used to prescribe the relative displacement of the nodes n_1 and n_2 . Given the considered boundary conditions (i.e., $d_1 = 0$), the constraint equation reads:

$$P^{k+1} = \Delta d_2^{k+1}(\delta\lambda^{k+1}) - \Delta\tau = \Delta d_2^k + \delta\lambda^{k+1}\delta d_{2,\text{I}}^{k+1} + \delta d_{2,\text{II}}^{k+1} - \Delta\tau = 0 \quad (74)$$

The loading factor increment $\delta\lambda^{k+1}$ can be thus calculated as:

$$\delta\lambda^{k+1} = \frac{\Delta\tau - a_0}{a_1} \quad (75)$$

with coefficients:

$$a_0 = \Delta d_2^k + \delta d_{2,\text{II}}^{k+1} \quad a_1 = \delta d_{2,\text{I}}^{k+1} \quad (76)$$

GS-CMSI. Finally, a global-scale indirect control method based on prescribing the strain rate of the weakened element is analyzed. Given the assumed loading/geometrical conditions and linear interpolation of the elemental displacement field, the constraint equation almost coincides with (74). Denoting with $h^w = x_2 - x_1$ the size of element w , one can write:

$$P^{k+1} = \Delta\varepsilon_w^{k+1}(\delta\lambda^{k+1}) - \Delta\tau = (\Delta d_2^k + \delta\lambda^{k+1}\delta d_{2,\text{I}}^{k+1} + \delta d_{2,\text{II}}^{k+1})/h^w - \Delta\tau = 0 \quad (77)$$

5.2.2. Results

Global responses. The global structural response is represented through the total applied force ($F = \lambda$) and sample elongation (ΔL). Figure 4 compares results obtained using the DS and GS formulations introduced above. A direct displacement controlled (DDC) simulation was also performed. For the sake of comparison, a fixed number of $N_\tau = 200$ pseudo-time steps was considered for each method. The corresponding $\Delta\tau$ values were chosen to obtain the same bar elongation ($\Delta L = 120 \mu\text{m}$) at the end of the simulation.

⁴Coefficients $a_{w,0}$ and $a_{w,1}$ were obtained by collecting terms in (70). Since $f_\alpha^{\text{elas}}(0) = \Delta e_w^k + \delta e_{w,\text{II}}^{k+1}$ and $\partial_{\delta\lambda} f_\alpha^{\text{elas}}(0) = \delta e_{w,\text{I}}^{k+1}$, it is straightforward checking that expressions (72) can be equivalently obtained from definitions (51).

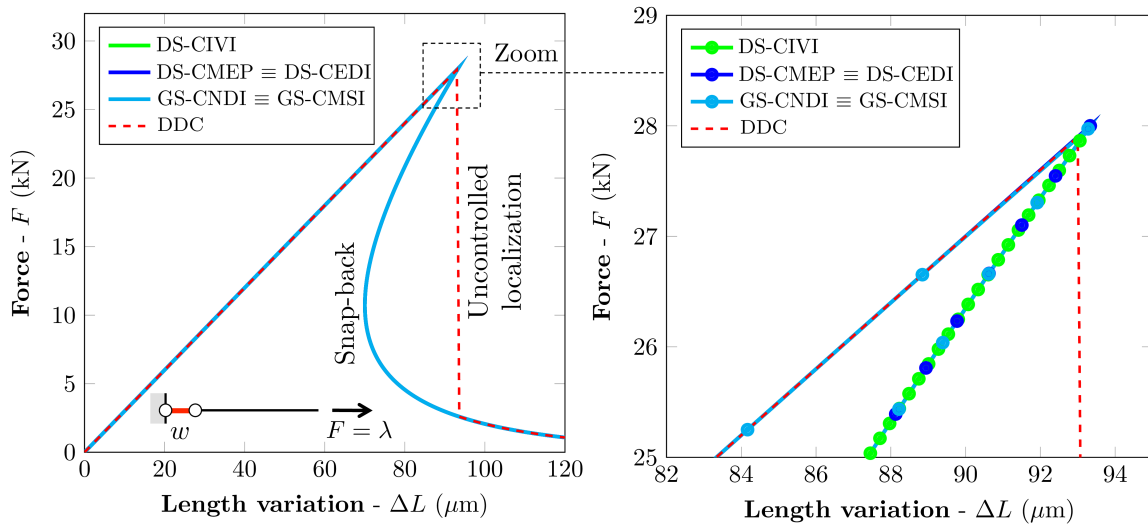


Figure 4: Bar under tension — Force-displacement responses obtained using the DS-CIVI, DS-CMEP, DS-CEDI, GS-CNDI, GS-CMSI and DDC formulations

As expected, the DDC loading does not allow to properly describe the force-displacement response in the phase post-peak of load. Indeed, once the localization condition is achieved, an uncontrolled elastic energy release occurs in the system and convergence is lost. This results in a sudden force reduction.

Conversely, indirect control methods allow to follow the structural response throughout the localization process in the whole range of ΔL levels. Concerning the DS constraints, given the adopted localization criterion, the first computed loading factor corresponds to the peak load. Once this condition is reached, the structural response becomes unstable and a clear snap-back is observed. Since a large number of pseudo-time steps is considered in simulations, the $(F, \Delta L)$ responses provided by the tested DS and GS formulations are very similar.

Total displacement, enhanced displacement and damage evolutions. To better illustrate the evolution of the localization process, Fig. 5 compares the pseudo-time evolutions of representative local quantities (the total displacement d_2 , the enhanced displacement e_w and the damage variable D_w) calculated using all the constraint equations previously introduced. As expected:

- (i) The enhanced displacement is always lower than the total displacement ($d_2 > e_w$) and progressively tends to its value when $D_w \rightarrow 1$. In this phase, no more load transfer is possible through the strong discontinuity. As a consequence, any displacement increase imposed to the system induces an increase in the displacement jump across the cracked element.
- (ii) When a DDC loading method is used, the global displacement evolves linearly (elastic phase) whereas the enhanced displacement remains null till $\sigma \leq \sigma_t$. Once the localization condition is attained, convergence is lost, an instantaneous damage increase occurs and abrupt variations of the total and enhanced displacements of the weakened element are obtained. This corresponds to the previously observed brutal decrease of the external force.
- (iii) When using path-following methods, the controlled quantities always evolve linearly with respect to the pseudo-time whereas other quantities non-linearly grow.

For the GS-CNDI (or equivalently the GS-CMSI) formulation, e_w and D_w remain null till the localization condition is attained. Then, they start increasing non-linearly up to the end of the simulation.

Different evolutions are observed when using the DS-CMEP (or equivalently the DS-CEDI) and DS-

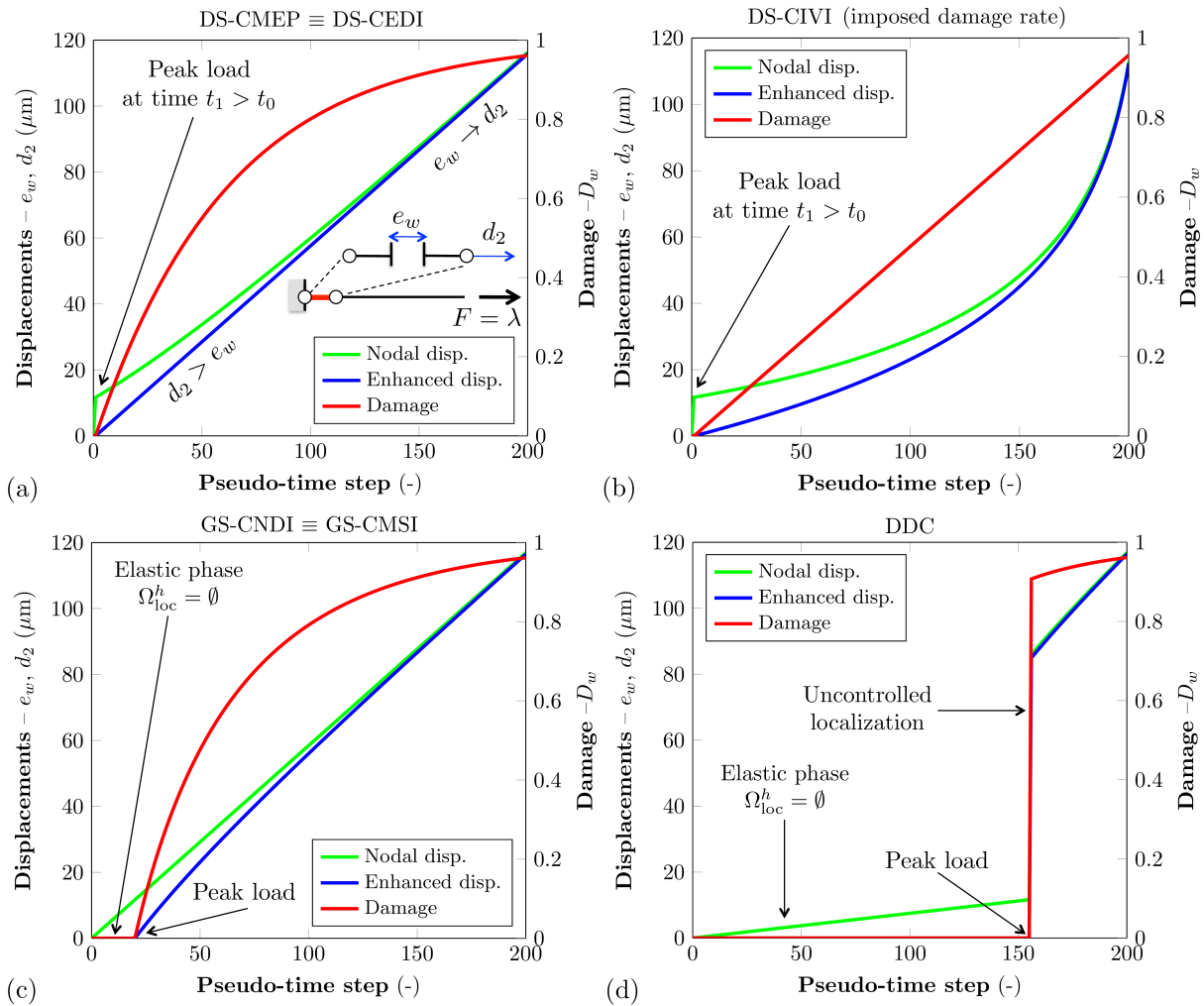


Figure 5: Bar under tension — Pseudo-time evolutions of the total displacement of node n_2 (d_2), of the enhanced displacement (e_w) computed at the gravity center of the weakened element and of the damage variable (D_w) computed at the same location: (a) DS-CMEP and DS-CEDI methods; (b) DS-CIVI method; (c) GS-CNDI and GS-CMSI methods; (d) DDC formulation

CIVI formulations. Indeed, provided the loading factor initiation procedure, d_2 sharply grows at the very beginning of the simulation (i.e., the elastic phase is not reproduced). The enhanced displacement then starts to gradually increase. In that phase, the total and enhanced displacements evolve non-linearly for both methods.

Their evolutions are, however, quite different. In particular, when using the DS-CIVI method, their rates of variation progressively increase when $D_w \rightarrow 1$. During this phase, controlling the simulation becomes more difficult because very small (imposed) damage increments (i.e., $\Delta\tau \rightarrow 0$) would be required in order to obtain an admissible displacement variations. The structural response may thus become unstable. Indeed, due to the bounded character of the damage variable (i.e., $D_w < 1$), controlling the damage growth makes difficult to reproduce the tail of the softening curve accurately. This issue will be more clear in the two-dimensional case test illustrated in the following section.

5.3. Two-dimensional test case: eccentrically perforated plate

A perforated plate $L = 2$ m in width (along the x -axis), $H = 2$ m in height (along the y -axis) and $T = 0.1$ m in thickness is submitted to a tensile loading in the horizontal direction (Fig. 6). The hole ($R = 0.5$ m in radius) is centered horizontally and eccentrically placed in the vertical direction. The computational domain is discretized through two finite element meshes comprising, respectively, 808 and 1338 CST elements. Horizontal displacements ($\mathbf{d}_{\text{imp}} = \mathbf{d}_{\text{imp},\lambda} = \lambda \mathbf{i}_x$, $\mathbf{i}_x = (1, 0)$) are imposed on the vertical right surface ($x = L$), whereas the left surface ($x = 0$) is blocked. Two-dimensional computations are performed under the plane stress assumption. Material parameters are: $E = 30$ GPa, $\nu = 0.2$ (Poisson's ratio), $\sigma_t = 3$ MPa and $G_f = 100$ N/m.

In order to compare the different methods, $\Delta\tau$ values were assigned to ensure approximately the same first computed enhanced displacement ($\approx 0.4 \mu\text{m}$) for each method. Given the localized nature of the cracking process at the strong discontinuity level and the illustrative purpose of the comparison, this criterion seemed acceptable and quite consistent from a physical viewpoint.

A very similar test was simulated by [13] and [10]. Accordingly, two vertical cracks are expected to propagate from the hole's boundary toward the upper and lower free-edges of the plate. Furthermore, since the hole is eccentrically placed, an unstable global response characterized by two snap-backs in the phase post-peak of load will be obtained.

5.3.1. Crack-path definition

Given the considered geometrical (symmetry) and loading conditions, the determination of the crack path is done a-priori by enforcing the crack propagation through the symmetry axis of the specimen. In other words, the Rankine's criterion is adopted to detect the onset of localization only. Once this condition is satisfied, elemental cracks are assumed vertically oriented ($\mathbf{n}_\alpha = \mathbf{i}_x$ for all $\alpha \in \Omega_{\text{loc}}^h$) and fixed.

Under more complex cracking conditions involving curved cracks, global/local crack tracking algorithms [58, 59, 60, 61, 62] should be used in order to ensure the continuity of the crack-path, thus avoiding stress-locking issues that may be encountered when no tracking methods are used. These formulations could be used in conjunction with path-following methods without requiring significant modifications to the numerical formulation. Although one could expect a moderate impact on the algorithmic robustness of the proposed path-following methods, such a study is not performed in this work for the sake of compactness.

5.3.2. Path-following constraint equations

DS-CMEP. Provided the considered loading conditions, the constraint equation is:

$$P^{k+1} = \max_{\alpha \in \Omega_{\text{loc}}^h} (e_{\alpha,n} + \Delta e_\alpha^k + \delta\lambda^{k+1} \delta e_{\alpha,\text{I}}^{k+1} + \delta e_{\alpha,\text{II}}^{k+1} - \kappa_{\alpha,n}) - \Delta\tau = 0 \quad (78)$$

A loading factor increment $\delta\lambda_\alpha^{k+1}$ is thus computed for each localized element as:

$$\delta\lambda_\alpha^{k+1} = \frac{\Delta\tau - a_{\alpha,0}}{a_{\alpha,1}} \quad (79)$$

where:

$$a_{\alpha,0} = e_{\alpha,n} + \Delta e_\alpha^k + \delta e_{\alpha,\text{II}}^{k+1} - \kappa_{\alpha,n} \quad a_{\alpha,1} = \delta e_{\alpha,\text{I}}^{k+1} \quad (80)$$

It should be noticed that, since localized elements can experience re-closure during crack propagation, $\kappa_{\alpha,n} \neq e_{\alpha,n}$. As a consequence, the DS-CMEP no more leads to exactly prescribe the rate of variation of the enhanced displacement field.

DS-CEDI. The constraint equation for controlling the enhanced displacement variation is written exactly as in (62). It can be, however, slightly simplified by observing that $\mathbf{c}_\alpha = \mathbf{n}_\alpha = \mathbf{i}_x$ for all $\alpha \in \Omega_{\text{loc}}^h$.

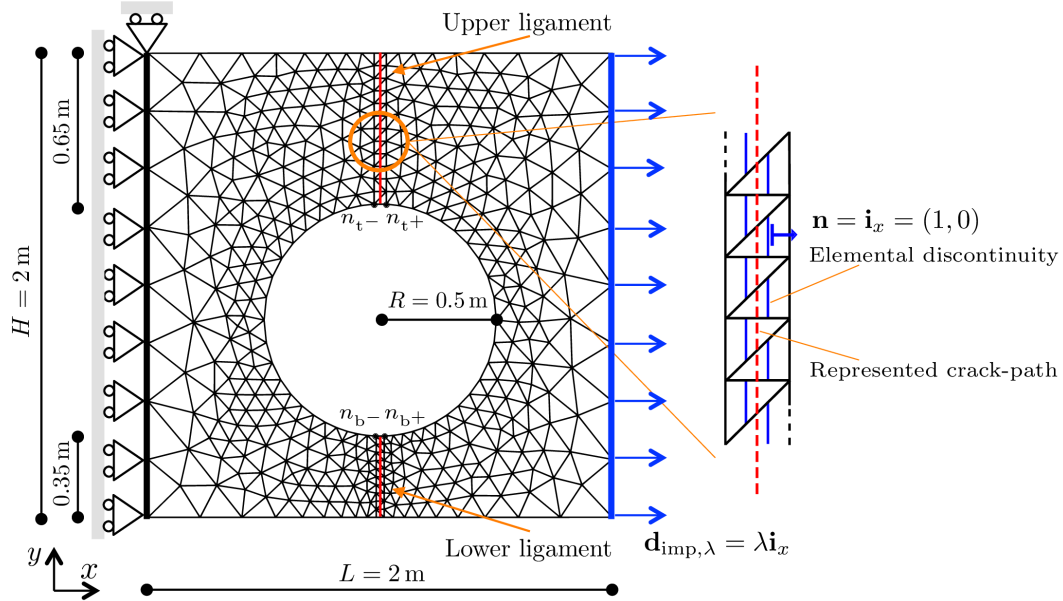


Figure 6: Perforated plate — Geometry of the computational domain, boundary/loading conditions, finite element discretization (808 CST elements), identification of the four nodes ($n_{t+}, n_{t-}, n_{b+}, n_{b-}$) used to compute Crack Opening Displacements ($\text{COD}_{\text{top}} = (d_{x,t+}^{k+1} + d_{x,t-}^{k+1})/2$, $\text{COD}_{\text{bottom}} = (d_{x,b+}^{k+1} + d_{x,b-}^{k+1})/2$, $\text{COD}_{\text{mean}} = (\text{COD}_{\text{top}} + \text{COD}_{\text{bottom}})/2$), and illustration of the chosen elemental strong discontinuities schematization

DS-CIVI. The path-following constraint on the rate of variation of the damage field can be written as:

$$P^{k+1} = \max_{\alpha \in \Omega_{\text{loc}}^h} (f_{\alpha}(e_{\alpha}^{k+1}(\delta\lambda_{\alpha}^{k+1}), \kappa_{\alpha}^{k+1}(D_{\alpha}^k + \Delta\tau - \Delta D_{\alpha}^k))) = 0 \quad (81)$$

Its resolution is performed through the same procedure as the DS-CMEP. Coefficients $a_{\alpha,0}$ and $a_{\alpha,1}$ figuring in (79) are now computed localized element by localized element according to expressions (73).

GS-CNDI. This method is used to control the mean Crack Opening Displacement (COD_{mean}) at the hole's boundary, where crack initiation is expected. This can be obtained by controlling the rate of variation of the mean relative horizontal displacements of two pairs of nodes (n_{t+}, n_{t-}) and (n_{b+}, n_{b-}) located close to the hole (Fig. 6). Following [6], the constraint equation reads:

$$P^{k+1} = \mathbf{p}^T \Delta \mathbf{d}^{k+1} - \Delta\tau = \mathbf{p}^T (\Delta \mathbf{d}^k + \delta \mathbf{d}_{\text{I}}^{k+1} \delta \lambda^{k+1} + \delta \mathbf{d}_{\text{II}}^{k+1}) - \Delta\tau = 0 \quad (82)$$

where \mathbf{p} is a selection vector defining a linear combination of the global DOFs. In the considered case, \mathbf{p} contains values $1/2$ and $-1/2$ at positions corresponding to the horizontal displacements of nodes (n_{t+}, n_{b+}) and (n_{t-}, n_{b-}) respectively, and is null elsewhere. As a consequence, $\delta \lambda^{k+1}$ can be computed from (75) with:

$$a_0 = \mathbf{p}^T (\Delta \mathbf{d}^k + \delta \mathbf{d}_{2,\text{II}}^{k+1}) \quad a_1 = \mathbf{p}^T \delta \mathbf{d}_{2,\text{I}}^{k+1} \quad (83)$$

GS-CMSI. Since strains are evaluated at the Gauss points level, this constraint equation can be written as:

$$P^{k+1} = \max_{\text{gp} \in \Omega_{\text{gp}}^h} (\mathbf{q}_{\text{gp}}^T \Delta \boldsymbol{\varepsilon}_{\text{gp}}^{k+1}) - \Delta\tau = 0 \quad (84)$$

where “gp” denotes now a Gauss integration point, Ω_{gp}^h is the set of all the integration points of the mesh, versor $\mathbf{q}_{\text{gp}} = \boldsymbol{\varepsilon}_{\text{gp},n} / \|\boldsymbol{\varepsilon}_{\text{gp},n}\|$ provides the direction of the strain vector at time t_n and:

$$\Delta \boldsymbol{\varepsilon}_{\text{gp}}^{k+1} = \mathbf{B}_{\text{gp}} \Delta \mathbf{d}^{k+1} = \mathbf{B}_{\text{gp}} (\Delta \mathbf{d}^k + \delta \mathbf{d}_{\text{II}}^{k+1}) + \delta \lambda^{k+1} \mathbf{B}_{\text{gp}} \delta \mathbf{d}_{\text{I}}^{k+1} \quad (85)$$

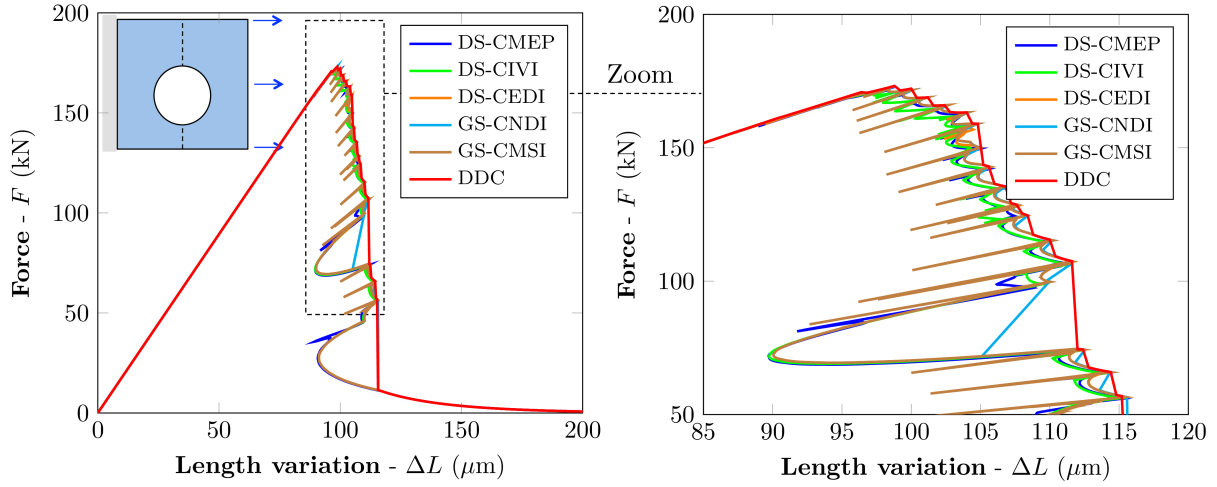


Figure 7: Perforated plate — Comparison among global responses obtained using the DS-CMEP, DS-CIVI, DS-CEDI, GS-CMSI, GS-CNDI and DDC formulations

with $\mathbf{B}_{\text{gp}} = \mathbf{B}(\mathbf{x}_{\text{gp}})$ denoting the strain-displacement matrix at the location \mathbf{x}_{gp} of $\text{gp} \in \Omega_{\text{gp}}^h$. The nested interval algorithm is still used, but equation (84) is now solved Gauss point by Gauss point. In this way, one has to solve n_{el} linear equations of the kind (79) with coefficients:

$$a_{\text{gp},0} = \mathbf{q}_{\text{gp}}^{\text{T}} \mathbf{B}_{\text{gp}} (\Delta \mathbf{d}^k + \delta \mathbf{d}_{2,\text{II}}^{k+1}) \quad a_{\text{gp},1} = \mathbf{q}_{\text{gp}}^{\text{T}} \mathbf{B}_{\text{gp}} \delta \mathbf{d}_{2,\text{I}}^{k+1} \quad (86)$$

5.3.3. Results

The global structural response is represented through the displacement ($\Delta L = \lambda$) of the bearing surface and the corresponding force (F). As shown in Fig. 7, a good agreement between the $(F, \Delta L)$ responses obtained through the path-following methods discussed above can be observed. The only exceptions are the GS-CNDI formulation (this aspect will be discussed in the following) and, as expected, the DDC method.

As already pointed out by several authors in other numerical contexts [13, 21, 10], the structural response is unstable and characterized by two clear snap-backs. Furthermore, small snap-backs corresponding to the strong discontinuity propagation through consecutive finite elements are also observed [63, 64, 65, 13].

Discontinuity-scale path-following constraints: representative response. For illustrating the main features of the observed structural behaviors, attention is first focused on the $(F, \Delta L)$ response computed through the DS-CMEP formulation (Fig. 8a). Figure 8b provides the discontinuity-scale damage field (D_{α}) for six representative phases of the simulation. The corresponding enhanced displacement (e_{α}) and damage distributions along a vertical line aligned with the mean-crack path (see Fig. 6) are also given in Fig. 9.

These results allow putting into evidence that once the peak load is reached, two cracks start propagating from the hole's boundary through the upper and lower ligaments. Since the hole is eccentrically placed, the lower crack reaches the bottom free-edge of the plate, while the tip of the other crack is still far from the upper boundary. Once this condition is attained, an elastic energy release takes place in the system and the structural response exhibits a first snap-back. Further loading steps correspond to the simultaneous opening of the lower crack and propagation of the upper one. When all the elements pertaining to the upper ligament are localized too, a novel elastic energy release occurs. This leads to a second snap-back. Finally, both cracks progressively open till the end of the simulation.

As mentioned before, small instabilities associated with elemental cracks activation are present in the structural response. These instabilities are thus strictly associated with the spatial discretization of the con-

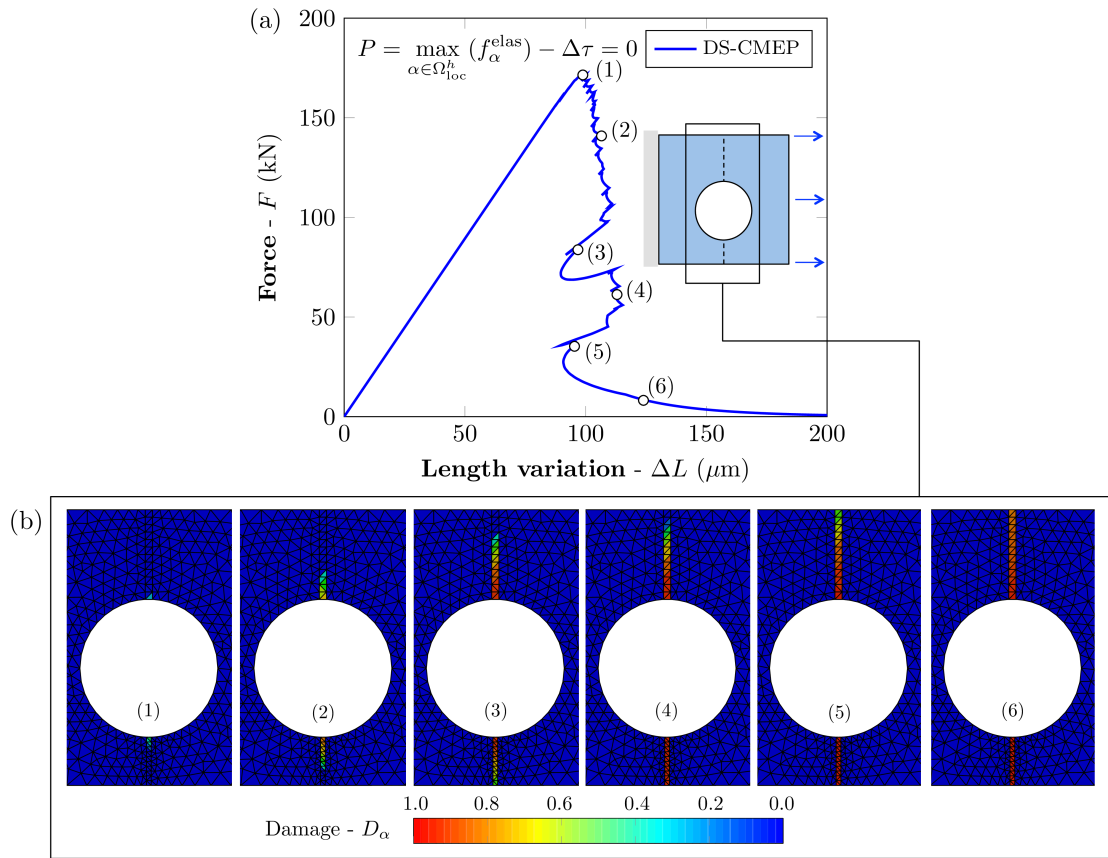


Figure 8: Perforated plate — Global sample response obtained using the DS-CMEP formulation (a) and damage fields (at the strong discontinuity level) corresponding to six phases of the simulation (b)

sidered problem. Figure 10 compares $(F, \Delta L)$ curves obtained considering two different mesh refinement levels. This illustration allows showing that the “rough” branch of the force-displacement curve progressively becomes smoother when refining the mesh, whereas the two major (physically motivated) snap-backs are preserved.

Discontinuity-scale path-following constraints: comparison among formulations. Very similar global and local responses can be obtained by controlling the simulation through the DS-CIVI (Fig. 11a) and DS-CEDI (Fig. 11b) methods. As shown in Fig. 11a, however, the DS-CIVI formulation does not allow to properly reproduce the structural response for high ΔL levels. This limitation stems directly from the upper-boundedness of the damage variable. Indeed, when all the finite elements pertaining to the upper and lower ligaments are localized and $D_{\min} = \min_{\alpha}(D_{\alpha}) > 1 - \Delta\tau$, finding an admissible solution (i.e., such that $D_{\alpha} \leq 1 \forall \alpha \in \Omega_{loc}^h$) to (81) becomes no more possible.⁵

This becomes even more clear when studying the pseudo-time evolutions of the maximum damage increase ($\Delta D_{\max} = \max_{\alpha}(\Delta D_{\alpha})$, Fig. 12a) and the maximum enhanced displacement increments ($\Delta e_{\max} = \max_{\alpha}(\Delta e_{\alpha})$, Fig. 12b). The evolutions of the maximum ($D_{\max} = \max_{\alpha}(D_{\alpha})$) and the minimum (D_{\min}) damage values over the upper and lower ligaments (for the three considered DS methods) are also given in Fig. 12c.⁶ As expected:

⁵To remove this limitation, one could imagine to progressively reduce $\Delta\tau$ from the initial (user-defined) value to zero. This kind of technique is not, however, implemented and studied in this work.

⁶Dimensionless pseudo-time t/t_{\max} is computed, for all control methods, as the ratio of the time step to the number of steps

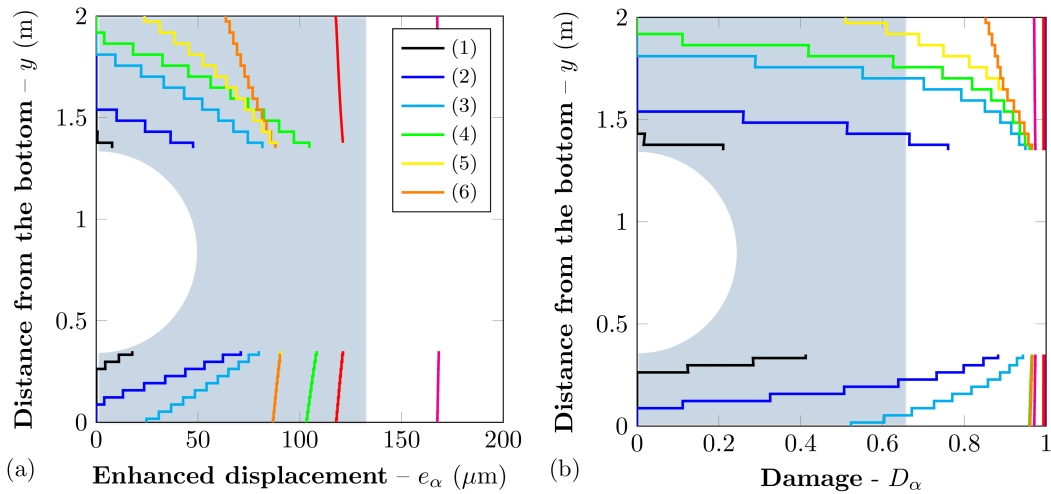


Figure 9: Perforated plate — Enhanced displacement e_α (a) and damage D_α (b) distributions along a vertical line aligned with the mean crack path (computation performed using the DS-CMEP formulation)

- (i) When using the DS-CIVI method, ΔD_{\max} remains almost constant and equal to the chosen $\Delta\tau$ value. Furthermore, when D_{\min} exceeds the limit value $1 - \Delta\tau$, convergence is lost and the simulation prematurely ends.
- (ii) This issue is not observed when controlling the simulation through unbounded variables (DS-CEDI and DS-CMEP formulations). Provided the chosen damage criterion function, the DS-CMEP path-following constraint almost leads to control the normal enhanced displacement variation. As a consequence, the DS-CMEP and DS-CEDI formulations provide very similar results. In both cases, Δe_{\max} (obtained/imposed) is approximately constant whereas the maximum damage nonlinearly evolves. At the end of the simulation, imposing almost constant enhanced displacement increments leads to compute progressively vanishing damage variations (i.e., $\Delta D_{\max} \rightarrow 0$ for $e_\alpha \rightarrow +\infty$).

Limited unwanted/parasite unloading-reloading paths can be observed in the global responses of Figs. 8a and 11a-b, as well as in the curves of Fig. 12. They are mainly associated with small instabilities occurring when elemental cracks propagate from a finite element to the adjacent one. From a numerical viewpoint, this issue could be further enhanced by the explicit procedure adopted to solve the path-following constraint equations at the elemental level, or by the use of too large $\Delta\tau$ values. Although a convergence study on the path-step length is not performed in this work, it should be noticed that higher the $\Delta\tau$, the lower the quality of the global response in representing the small instabilities mentioned above.

A further possible explication for these elastic unloadings should be mentioned for the DS-CEDI method. Indeed, since localized elements may experience crack re-closure during the strong discontinuity propagation, increases in the enhanced displacement may be predicted both in the elastic and dissipative regimes. Such issue does not affect the DS-CMEP and DS-CIVI formulations, since they are designed to select dissipative solutions only.

Discontinuity-scale vs global-scale path-following constraints. The interest of using DS constraints in the E-FEM context becomes more clear when comparing previous responses with those obtained through the GS-CMSI and GS-CNDI methods. As shown in Fig. 13, these formulations are not fully satisfactory for

needed to attain $\Delta L = 200 \mu\text{m}$. The sole exception concerns the DS-CIVI method. Since the simulation stops prematurely, t/t_{\max} is evaluated as the ratio of the time step (t) to the total number of computed time steps, multiplied by the ratio of the maximum attained ΔL level to $200 \mu\text{m}$.

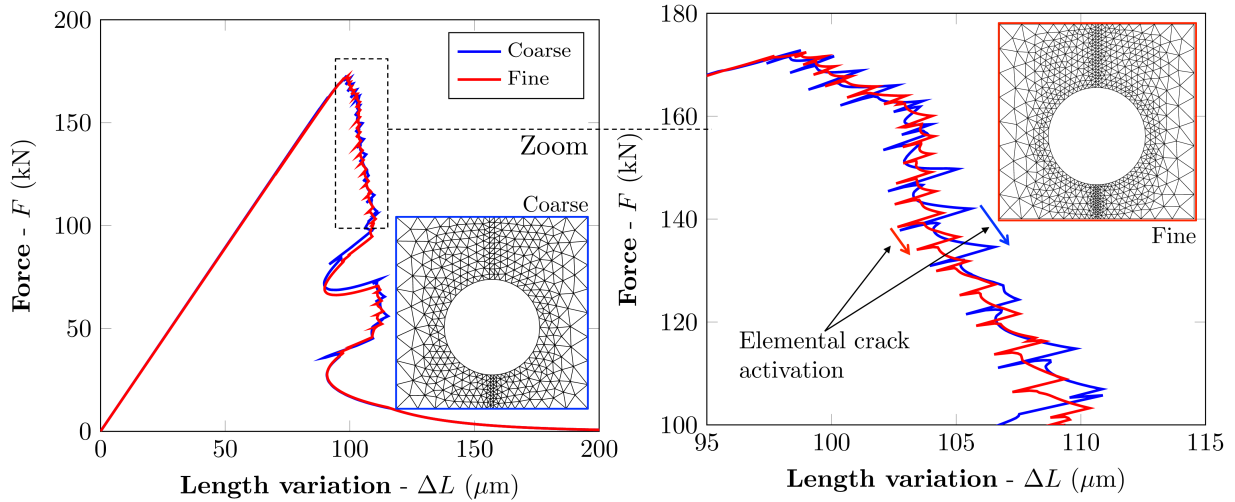


Figure 10: Perforated plate — Global sample responses obtained using the DS-CMEP formulation for two different finite element meshes containing 34 (coarse mesh) and 72 (finer mesh) elements along the upper and lower ligaments. The total number of finite elements is 808 and 1338, respectively

different reasons. In particular, due to the chosen control variable, the GS-CNDI method allows describing local instabilities due to elemental cracks localization. However, the two snap-backs corresponding to the complete localization of the upper and lower cracks are not followed properly. At the price of a more time expensive computation (due to the nested interval algorithm) the GS-CMSI formulation yields improving this aspect. However, since solutions can be found in both elastic and dissipative regimes [13], several elastic unloading-reloading equilibrium paths are obtained.

These “less controlled” responses are also clear when analyzing the pseudo-time evolutions of ΔD_{\max} and Δe_{\max} throughout the simulations (Fig. 14). In both cases, these quantities exhibit more important variations than those observed using discontinuity-scale constraints. In particular:

- (i) For the GS-CNDI formulation, ΔD_{\max} ranges between approximately null values and about 0.95. The higher damage variations are attained in correspondence of the abrupt force decreases observed in the structural responses.
- (ii) In the case of the GS-CMSI, ΔD_{\max} and Δe_{\max} evolve in a more controlled way. The presence of non-dissipative unloading-reloading equilibrium paths is, however, again clear: null maximum damage increases are obtained ($\Delta D_{\max} = 0$) for several time intervals. Elastic unloading paths induce abrupt reductions in Δe_{\max} , whereas elastic reloading take place with approximately constant enhanced displacement variations ($\Delta e_{\max} = \text{cst.}$). This clearly put into evidence that the enhanced displacement of the elemental discontinuity experiencing $\Delta D_{\max} = 0$ increases linearly, following the damaged elastic branch of the traction separation-law.

Another comparison can be established by analyzing the $\text{COD}_{\text{mean}} = \mathbf{p}^T \Delta \mathbf{d}$ evolution respect to the sample elongation. As shown in Fig. 15, when snap-backs occur, ΔL and COD_{mean} both decrease for all the control methods. The only exception is the GS-CNDI method, because (82) prescribes that $\Delta(\text{COD}_{\text{mean}}) = \Delta\tau > 0$. Since the COD_{mean} variation is not allowed to become negative, the capability of the GS-CNDI method to follow these instabilities cannot therefore be enhanced by reducing $\Delta\tau$. The only way for improving numerical results could consist, in that case, in considering a different set of DOFs to compute the controlled displacement variable. However, such a choice is not straightforward, because the *a-priori* knowledge of the cracks opening mechanism is required.

Previous considerations can be further corroborated by studying the pseudo-time evolutions of COD_{top} ,

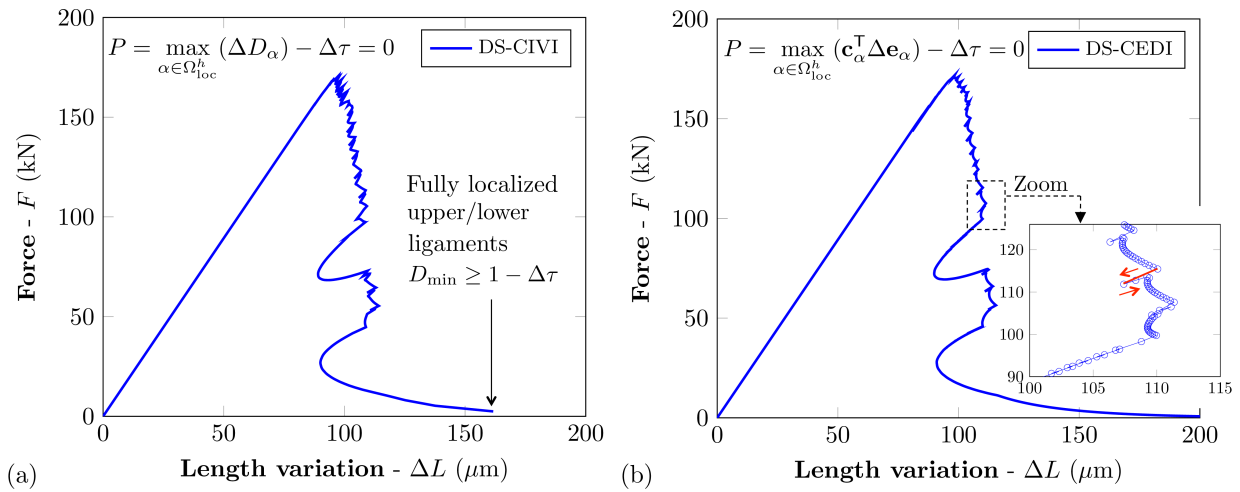


Figure 11: Perforated plate — Global sample responses obtained through the DS-CIVI (a) and DS-CEDI (b) formulations

COD_{bottom} and COD_{mean} (Fig. 16). The sole GS-CNDI and GS-CMSI methods are considered for the sake of simplicity. As expected, COD_{bottom} is larger than COD_{top} for both methods in the first phase of the test. When using the GS-CMSI method, the two physically motivated snap-backs correspond to a simultaneous decrease in the COD measures. In other words, both cracks re-close when snap-backs occur. This is not, however, possible when using the GS-CNDI method, because fulfilling the path-following constraint (82) implies that at least one COD measure continues increasing throughout the entire deformation process.

6. Conclusive remarks

Path-following methods for post-critical structural responses induced by the localization of strong discontinuities were discussed in the framework of the E-FEM. Given the static condensation of the enhanced fields at the elemental level, we showed that additively decomposing the nodal displacement field – as it is classically done in path-following methods – leads to a similar decomposition of the enhanced displacement field. Thanks to the enriched kinematics description proper to the E-FEM, it is therefore possible to formulate constraint equations where the controlled quantities refer to the global problem (nodal displacements, total strains, ...) as well as the discontinuity-scale problem (displacement jump, internal variables of the traction-separation law, ...). In this way, it is possible to control the localization process occurring at the embedded discontinuity level directly.

Several Discontinuity-Scale (DS) constraint equations were presented and their numerical implementation, based on an operator splitting method, was discussed (DS-CMEP, DS-CIVI and DS-CEDI methods). The simulation of simple structural test cases involving unstable structural responses allowed validating the proposed formulations. Although attention was mainly focused on DS formulations, two well known Global-Scale (GS) path-following constraints (commonly used in nonlinear finite element simulations) were considered for the sake of comparison. A deep comparative study of the illustrated formulations is still needed. However, these first analyses showed that DS constraints are quite effective in E-FEM simulations. In particular, despite what is obtained when considering modified arc-length algorithms based upon prescribing a combination of global DOFs [6], or when controlling the maximum strain increment over the computational domain [8, 9, 10], it seems possible to obtain a more accurate representation of dissipative equilibrium solutions.

Further works are needed in order to study these DS methods and their implementation. Indeed, in the present work, explicit root-finding algorithms were used to solve the constraint equations at the elemental

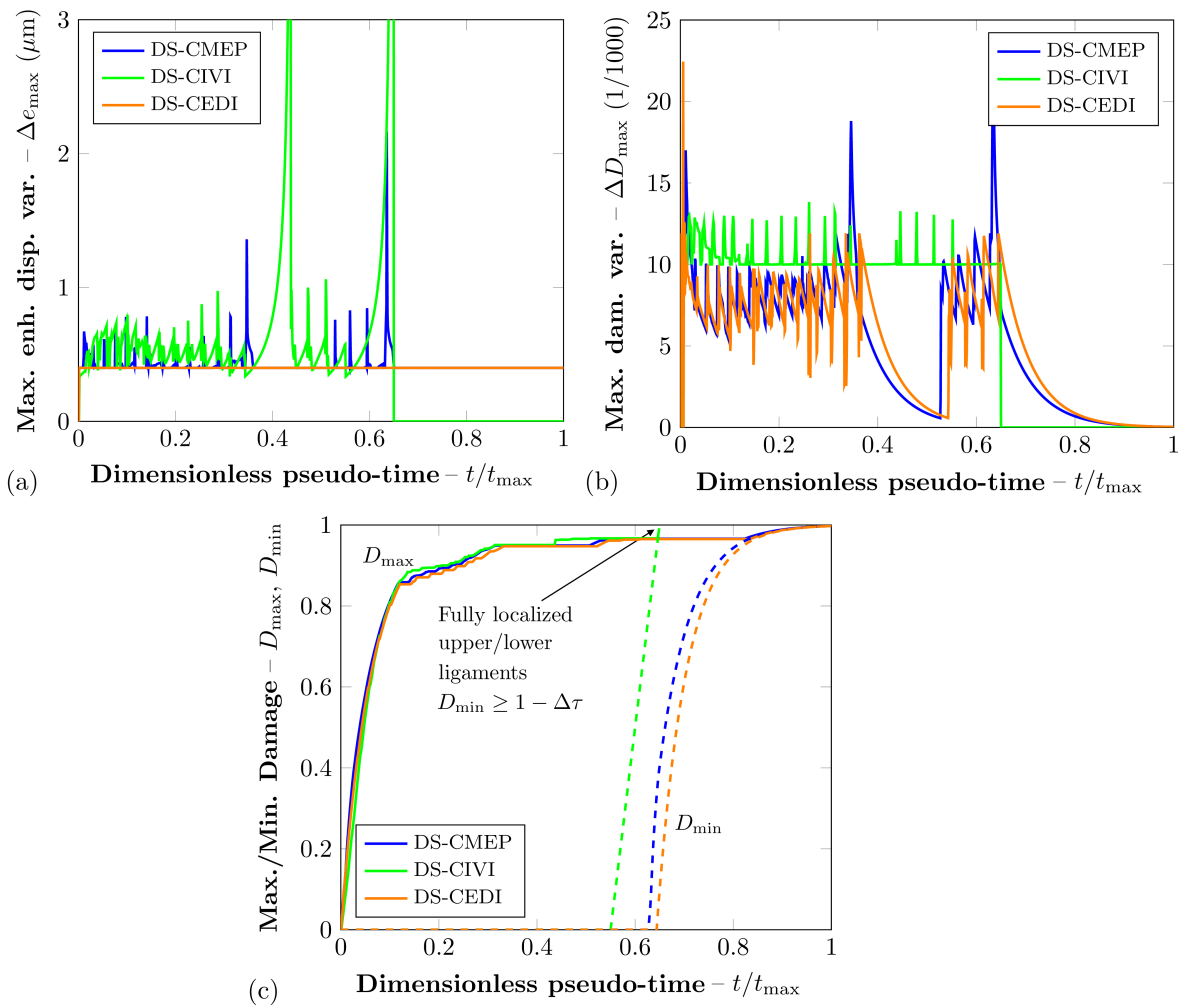


Figure 12: Perforated plate — Pseudo-time evolutions of the maximum damage variation (ΔD_{\max}) (a), the maximum enhanced displacement variation (Δe_{\max}) (b), the maximum (D_{\max}) and minimum (D_{\min}) damage (c) computed through the DS-CMEP, DS-CIVI and DS-CEDI formulations

level. Since such a choice could partly explain some (limited) unwanted loading-unloading paths observed in the global response of the holed plate (second test case), one should also investigate implicit methods. At the price of increasing the computational cost associated with the resolution of the control equation, this could increase accuracy in the determination of the dissipative solution. A convergence analysis with respect to the loading parameter $\Delta\tau$ could also be extremely useful to achieve this goal. Finally, the study of more complex quasi-static strain localization problems involving curved, branching and geometrically complex cracks should be performed.

Acknowledgements

This work was supported by the SEISM Institute (<http://www.institut-seism.fr>). The authors declare no potential conflicts of interest with respect to the research, authorship, and/or publication of this article. The authors gratefully acknowledge the anonymous Reviewers for their insightful comments and suggestions on the manuscript.

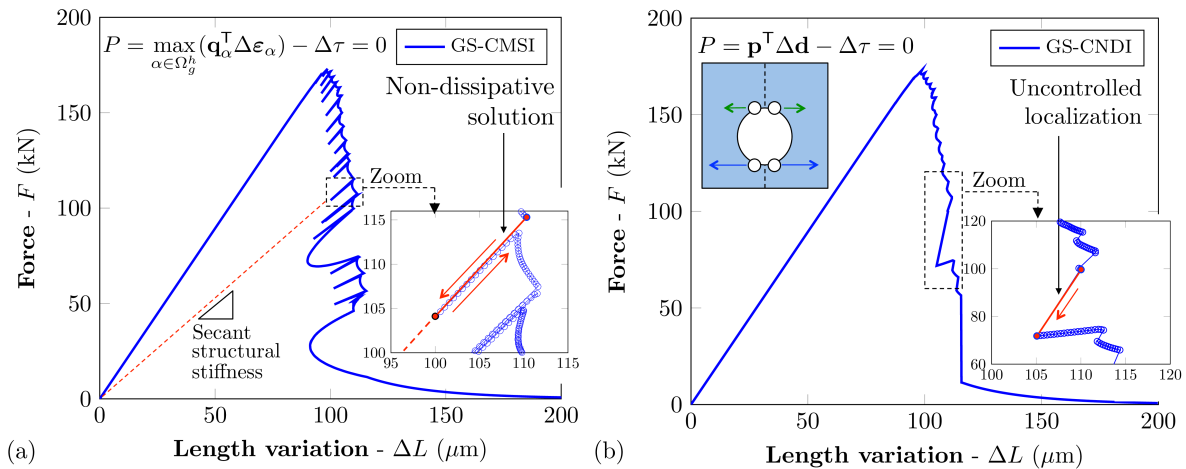


Figure 13: Perforated plate — Global sample response obtained through the global-scale GS-CMSI (a) and GS-CNDI (b) formulations

References

- [1] Zdenek P Bazant. Mechanics of distributed cracking. *Appl. Mech. Rev.*, 39(5):675–705, 1986.
- [2] R De Borst, M A Crisfield, J J C Remmers, and C V Verhoosel. *Nonlinear finite element analysis of solids and structures*. John Wiley & Sons, 2012.
- [3] E Riks. *The Application of Newton's Method to the Problem of Elastic Stability*. American Society of Mechanical Engineers, 1972.
- [4] M A Crisfield. A fast incremental/iterative solution procedure that handles snap-through. *Computers & Structures*, 13(1-3):55–62, 1981.
- [5] E Ramm. Strategies for tracing the nonlinear response near limit points. In *Nonlinear finite element analysis in structural mechanics*, pages 63–89. Springer, 1981.
- [6] R De Borst. Computation of post-bifurcation and post-failure behavior of strain-softening solids. *Computers & Structures*, 25(2):211–224, 1987.
- [7] I M May and Y Duan. A local arc-length procedure for strain softening. *Computers & structures*, 64(1):297–303, 1997.
- [8] Zhen Chen and Howard L Schreyer. A numerical solution scheme for softening problems involving total strain control. *Computers & Structures*, 37(6):1043–1050, 1990.
- [9] M G D Geers. Enhanced solution control for physically and geometrically non-linear problems. Part I – the subplane control approach. *International Journal for Numerical Methods in Engineering*, 46(2):177–204, 1999.
- [10] Tanja Pohl, Ekkehard Ramm, and Manfred Bischoff. Adaptive path following schemes for problems with softening. *Finite Elements in Analysis and Design*, 86:12 – 22, 2014. ISSN 0168-874X. doi: <https://doi.org/10.1016/j.finel.2014.02.005>. URL <http://www.sciencedirect.com/science/article/pii/S0168874X14000225>.
- [11] Miguel A. Gutiérrez. Energy release control for numerical simulations of failure in quasi-brittle solids. *Communications in Numerical Methods in Engineering*, 20(1):19–29, 2004. ISSN 1099-0887. doi: 10.1002/cnm.649. URL <http://dx.doi.org/10.1002/cnm.649>.
- [12] Clemens V. Verhoosel, Joris J. C. Remmers, and Miguel A. Gutiérrez. A dissipation-based arc-length method for robust simulation of brittle and ductile failure. *International Journal for Numerical Methods in Engineering*, 77(9):1290–1321, 2009. ISSN 1097-0207. doi: 10.1002/nme.2447. URL <http://dx.doi.org/10.1002/nme.2447>.
- [13] E Lorentz and P Badel. A new path-following constraint for strain-softening finite element simulations. *International journal for numerical methods in engineering*, 60(2):499–526, 2004.
- [14] N. Singh, C.V. Verhoosel, R. de Borst, and E.H. van Brummelen. A fracture-controlled path-following technique for phase-field modeling of brittle fracture. *Finite Elements in Analysis and Design*, 113:14 – 29, 2016. ISSN 0168-874X. doi: <https://doi.org/10.1016/j.finel.2015.12.005>. URL <http://www.sciencedirect.com/science/article/pii/S0168874X15001870>.
- [15] Andjelka Stanić and Boštjan Brank. A path-following method for elasto-plastic solids and structures based on control of plastic dissipation and plastic work. *Finite Elements in Analysis and Design*, 123:1 – 8, 2017. ISSN 0168-874X. doi: <https://doi.org/10.1016/j.finel.2016.09.005>. URL <http://www.sciencedirect.com/science/article/pii/S0168874X16303456>.
- [16] Ettore Barbieri, Federica Ongaro, and Nicola Maria Pugno. A j-integral-based arc-length solver for brittle and ductile crack propagation in finite deformation-finite strain hyperelastic solids with an application to graphene kirigami. *Computer Methods in Applied Mechanics and Engineering*, 315:713 – 743, 2017. ISSN 0045-7825. doi: <https://doi.org/10.1016/j.cma.2016.10.043>. URL <http://www.sciencedirect.com/science/article/pii/S0045782516307897>.
- [17] Davide Bellora and Riccardo Vescovini. Hybrid geometric-dissipative arc-length methods for the quasi-static analysis of delamination problems. *Computers & Structures*, 175:123 – 133, 2016. ISSN 0045-7949. doi: <https://doi.org/10.1016/j>

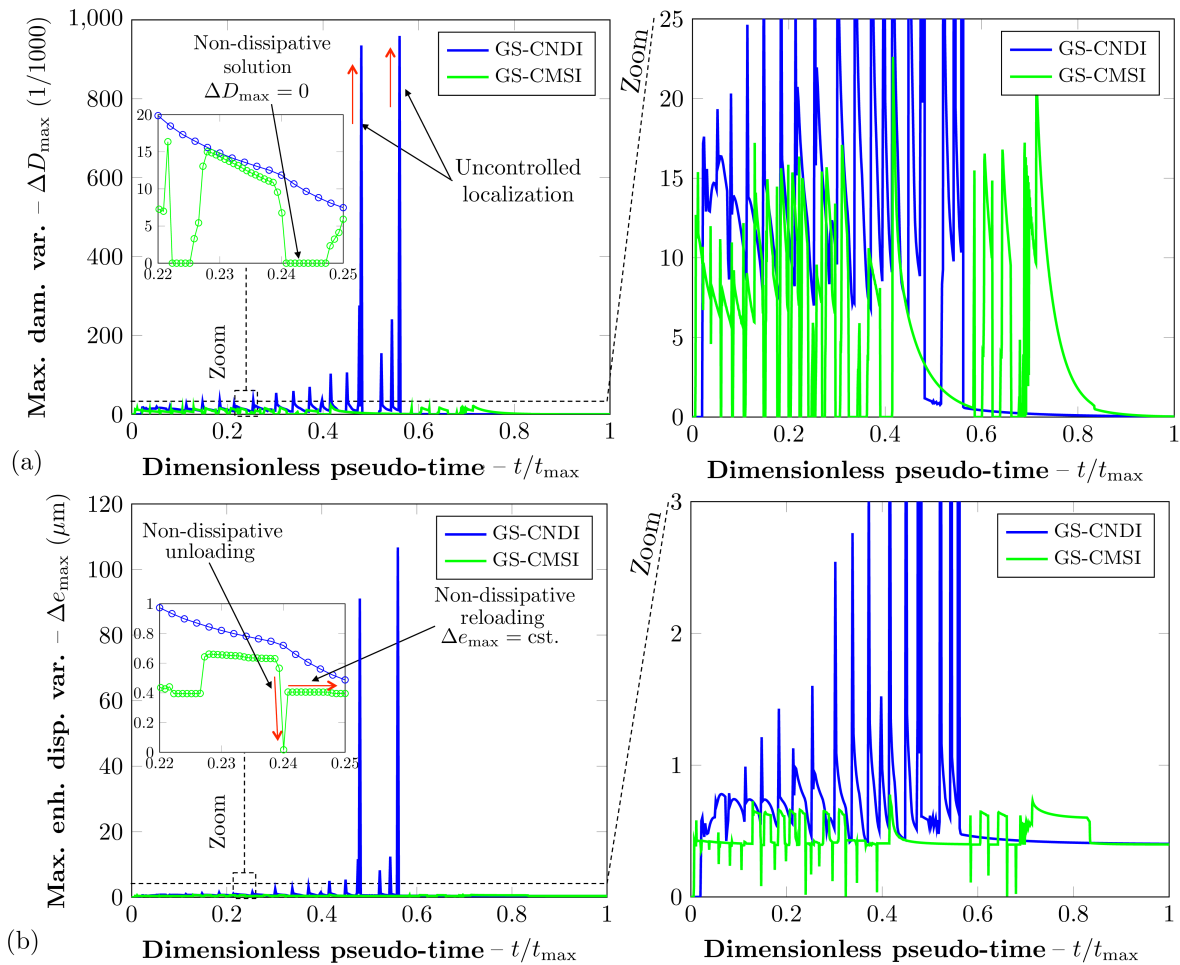


Figure 14: Perforated plate – Pseudo-time evolutions of the maximum damage variation (ΔD_{\max}) and the maximum enhanced displacement ($\Delta \epsilon_{\max}$) variation computed through the GS-CNDI (a) and GS-CMSI (b) formulations

- compstruc.2016.07.002. URL <http://www.sciencedirect.com/science/article/pii/S0045794916306022>.
- [18] Giuseppe Rastiello, Cédric Giry, Fabrice Gatuingt, and Rodrigue Desmorat. From diffuse damage to strain localization from an eikonal non-local (enl) continuum damage model with evolving internal length. *Computer Methods in Applied Mechanics and Engineering*, 331:650 – 674, 2018. ISSN 0045-7825. doi: <https://doi.org/10.1016/j.cma.2017.12.006>. URL <http://www.sciencedirect.com/science/article/pii/S0045782517307582>.
- [19] Kévin Moreau, Nicolas Moës, Nicolas Chevaugnon, and Alexis Salzman. Concurrent development of local and non-local damage with the thick level set approach: Implementation aspects and application to quasi-brittle failure. *Computer Methods in Applied Mechanics and Engineering*, 327:306 – 326, 2017. ISSN 0045-7825. doi: <https://doi.org/10.1016/j.cma.2017.08.045>. URL <http://www.sciencedirect.com/science/article/pii/S0045782517306230>. Advances in Computational Mechanics and Scientific Computation—the Cutting Edge.
- [20] G. Alfano and M. A. Crisfield. Solution strategies for the delamination analysis based on a combination of local-control arc-length and line searches. *International Journal for Numerical Methods in Engineering*, 58(7):999–1048, 2003. ISSN 1097-0207. doi: 10.1002/nme.806. URL <http://dx.doi.org/10.1002/nme.806>.
- [21] Patrick Massin, Guilhem Ferté, Axelle Caron, and Nicolas Moës. Pilotage du chargement en formulation x-fem: application aux lois cohésives. In *10e colloque national en calcul des structures*, pages Clé–USB, 2011.
- [22] J. Oliver, A.E. Huespe, and J.C. Cante. An implicit/explicit integration scheme to increase computability of non-linear material and contact/friction problems. *Computer Methods in Applied Mechanics and Engineering*, 197(21):1865 – 1889, 2008. ISSN 0045-7825. doi: <https://doi.org/10.1016/j.cma.2007.11.027>. URL <http://www.sciencedirect.com/science/article/pii/S0045782507004756>.
- [23] Boštjan Brank, Andjelka Stanić, and Adnan Ibrahimbegovic. A path-following method based on plastic dissipation control. In *Computational Methods for Solids and Fluids*, pages 29–47. Springer, 2016.

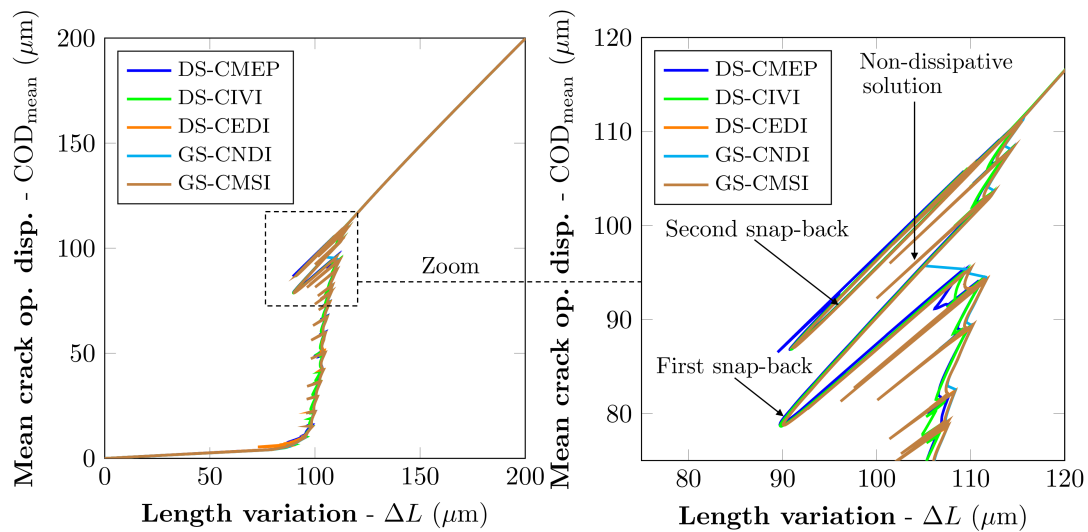


Figure 15: Perforated plate – Mean COD evolutions with respect to the sample elongation (ΔL) obtained through the DS-CMEP, DS-CIVI, DS-CEDI, GS-CMSI and GS-CNDI formulations

- [24] Fabien Cazes, Günther Meschke, and Meng-Meng Zhou. Strong discontinuity approaches: An algorithm for robust performance and comparative assessment of accuracy. *International Journal of Solids and Structures*, 96:355 – 379, 2016. ISSN 0020-7683. doi: <https://doi.org/10.1016/j.ijsolstr.2016.05.016>. URL <http://www.sciencedirect.com/science/article/pii/S0020768316300956>.
- [25] J C Simo, J Oliver, and F Armero. An analysis of strong discontinuities induced by strain-softening in rate-independent inelastic solids. *Computational mechanics*, 12(5):277–296, 1993.
- [26] J C Simo and J Oliver. A new approach to the analysis and simulation of strain softening in solids. *Fracture and damage in quasibrittle structures*, pages 25–39, 1994.
- [27] F Armero and K Garikipati. An analysis of strong discontinuities in multiplicative finite strain plasticity and their relation with the numerical simulation of strain localization in solids. *International Journal of Solids and Structures*, 33(20):2863–2885, 1996.
- [28] J Oliver, M Cervera, and O Manzoli. Strong discontinuities and continuum plasticity models: the strong discontinuity approach. *International journal of plasticity*, 15(3):319–351, 1999.
- [29] J Oliver, A E Huespe, E Samaniego, and E W V Chaves. Continuum approach to the numerical simulation of material failure in concrete. *International Journal for Numerical and Analytical Methods in Geomechanics*, 28(7-8):609–632, 2004.
- [30] J Oliver and A E Huespe. Continuum approach to material failure in strong discontinuity settings. *Computer Methods in Applied Mechanics and Engineering*, 193(30):3195–3220, 2004.
- [31] T Belytschko and T Black. Elastic crack growth in finite elements with minimal remeshing. *International journal for numerical methods in engineering*, 45(5):601–620, 1999.
- [32] J Dolbow and T Belytschko. A finite element method for crack growth without remeshing. *International journal for numerical methods in engineering*, 46(1):131–150, 1999.
- [33] J Dolbow, N Moës, and T Belytschko. Discontinuous enrichment in finite elements with a partition of unity method. *Finite elements in analysis and design*, 36(3):235–260, 2000.
- [34] N Moës and T Belytschko. Extended finite element method for cohesive crack growth. *Engineering fracture mechanics*, 69(7):813–833, 2002.
- [35] Eduardo N. Dvorkin, Alberto M. Cuitiño, and Gustavo Gioia. Finite elements with displacement interpolated embedded localization lines insensitive to mesh size and distortions. *International Journal for Numerical Methods in Engineering*, 30(3):541–564, 8 1990. ISSN 1097-0207. doi: 10.1002/nme.1620300311. URL <http://https://doi.org/10.1002/nme.1620300311>.
- [36] M Jirásek. Comparative study on finite elements with embedded discontinuities. *Computer methods in applied mechanics and engineering*, 188(1):307–330, 2000.
- [37] Garth N Wells and LJ Sluys. A new method for modelling cohesive cracks using finite elements. *International Journal for Numerical Methods in Engineering*, 50(12):2667–2682, 2001.
- [38] GN Wells and LJ Sluys. Three-dimensional embedded discontinuity model for brittle fracture. *International Journal of Solids and Structures*, 38(5):897–913, 2001.
- [39] Hai-Chang Hu. On some variational principles in the theory of elasticity and the theory of plasticity. 1955.
- [40] K Washizu. *Variational methods in elasticity and plasticity*. Pergamon press, 1975.
- [41] C. Linder and F. Armero. Finite elements with embedded strong discontinuities for the modeling of failure in solids.

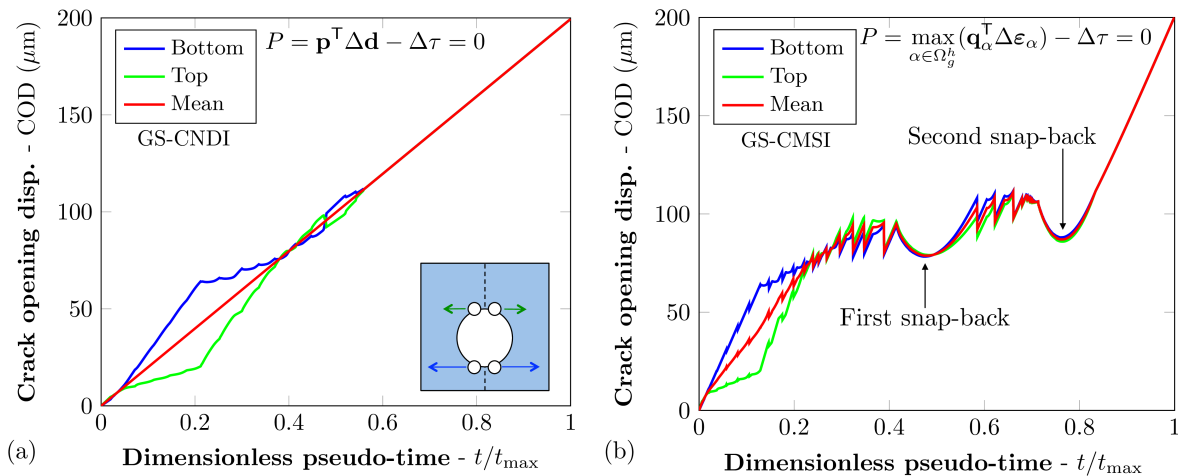


Figure 16: Perforated plate – Pseudo-time evolutions of COD_{top} , COD_{bottom} and COD_{mean} obtained through the GS-CNDI (a) and GS-CMSI (b) formulations

International Journal for Numerical Methods in Engineering, 72(12):1391–1433, 2007.

[42] F. Armero and C. Linder. New finite elements with embedded strong discontinuities in the finite deformation range. *Computer Methods in Applied Mechanics and Engineering*, 197(33-40):3138–3170, 2008.

[43] G. Rastiello, C. Boulay, S. Dal Pont, J.L. Tailhan, and P. Rossi. Real-time water permeability evolution of a localized crack in concrete under loading. *Cement and Concrete Research*, 56:20 – 28, 2014. ISSN 0008-8846. doi: <https://doi.org/10.1016/j.cemconres.2013.09.010>. URL <http://www.sciencedirect.com/science/article/pii/S0008884613001968>.

[44] Giuseppe Rastiello, Jean-Louis Tailhan, Pierre Rossi, and Stefano Dal Pont. Macroscopic probabilistic cracking approach for the numerical modelling of fluid leakage in concrete. *Annals of Solid and Structural Mechanics*, 7(1):pp.1–16, January 2015. doi: 10.1007/s12356-015-0038-6. URL <https://hal.archives-ouvertes.fr/hal-01471670>.

[45] D Brancherie. *Modèles continus et "discrets" pour les problèmes de localisation et de rupture fragile et/ou ductile*. PhD thesis, 2003.

[46] C. Callari and F. Armero. Finite element methods for the analysis of strong discontinuities in coupled poro-plastic media. *Computer Methods in Applied Mechanics and Engineering*, 191(39):4371 – 4400, 2002. ISSN 0045-7825. doi: [https://doi.org/10.1016/S0045-7825\(02\)00374-2](https://doi.org/10.1016/S0045-7825(02)00374-2). URL <http://www.sciencedirect.com/science/article/pii/S0045782502003742>.

[47] C. Callari and A. Lupoi. *Localization Analysis in Dilatant Elasto-Plastic Solids by a Strong-Discontinuity Method*, pages 121–132. Springer Berlin Heidelberg, Berlin, Heidelberg, 2004. ISBN 978-3-540-45287-4. doi: 10.1007/978-3-540-45287-4_8. URL https://doi.org/10.1007/978-3-540-45287-4_8.

[48] J. Oliver, A.E. Huespe, M.D.G. Pulido, and E. Chaves. From continuum mechanics to fracture mechanics: the strong discontinuity approach. *Engineering Fracture Mechanics*, 69(2):113 – 136, 2002. ISSN 0013-7944. doi: [https://doi.org/10.1016/S0013-7944\(01\)00060-1](https://doi.org/10.1016/S0013-7944(01)00060-1). URL <http://www.sciencedirect.com/science/article/pii/S0013794401000601>.

[49] J Alfaiate, G N Wells, and L J Sluys. On the use of embedded discontinuity elements with crack path continuity for mode-I and mixed-mode fracture. *Engineering Fracture Mechanics*, 69(6):661–686, 2002.

[50] M Cervera, L Pelà, R Clemente, and P Roca. A crack-tracking technique for localized damage in quasi-brittle materials. *Engineering Fracture Mechanics*, 77(13):2431–2450, 2010.

[51] Kenneth Runesson, Niels Saabye Ottosen, and Perić Dunja. Discontinuous bifurcations of elastic-plastic solutions at plane stress and plane strain. *International Journal of Plasticity*, 7(1-2):99–121, 1991.

[52] H B Hellweg and M A Crisfield. A new arc-length method for handling sharp snap-backs. *Computers & Structures*, 66(5):704–709, 1998.

[53] N. Moës, C. Stolz, P.-E. Bernard, and N. Chevaugeon. A level set based model for damage growth: The thick level set approach. *International Journal for Numerical Methods in Engineering*, 86(3):358–380, 2011. ISSN 1097-0207. doi: 10.1002/nme.3069. URL <http://dx.doi.org/10.1002/nme.3069>.

[54] Benjamin Richard, Giuseppe Rastiello, Cédric Giry, Francesco Riccardi, Romili Paredes, Eliass Zafati, Santosh Kakarla, and Chaymaa Lejouad. Castlab: an object-oriented finite element toolbox within the matlab environment for educational and research purposes in computational solid mechanics. *Advances in Engineering Software*, 2018.

[55] Konstantinos N. Anyfantis and Nicholas G. Tsouvalis. A novel traction-separation law for the prediction of the mixed mode response of ductile adhesive joints. *International Journal of Solids and Structures*, 49(1):213 – 226, 2012. ISSN 0020-7683. doi: <https://doi.org/10.1016/j.ijsolstr.2011.10.001>. URL <http://www.sciencedirect.com/science/article/pii/S0020768311003313>.

[56] Benjamin Richard, Ejona Kishta, Cédric Giry, and Frédéric Ragueneau. Strong discontinuity analysis of a class of anisotropic continuum damage constitutive models—part i: Theoretical considerations. *Mechanics Research Commu-*

- nications*, 86:32–36, 2017.
- [57] Ejona Kishta, Benjamin Richard, Cédric Giry, and Frédéric Ragueneau. Strong discontinuity analysis of a class of anisotropic continuum damage constitutive models—part ii: Concrete material application. *Mechanics Research Communications*, 86:27–31, 2017.
- [58] J Oliver, A E Huespe, E Samaniego, and E W V Chaves. On strategies for tracking strong discontinuities in computational failure mechanics. In *Fifth World Congress on Computational Mechanics*, 2002.
- [59] G Ventura, E Budyn, and T Belytschko. Vector level sets for description of propagating cracks in finite elements. *International Journal for Numerical Methods in Engineering*, 58(10):1571–1592, 2003.
- [60] J Mosler and G Meschke. Embedded crack vs. smeared crack models: a comparison of elementwise discontinuous crack path approaches with emphasis on mesh bias. *Computer Methods in Applied Mechanics and Engineering*, 193(30):3351–3375, 2004.
- [61] G Meschke and P Dumstorff. Energy-based modeling of cohesive and cohesionless cracks via X-FEM. *Computer Methods in Applied Mechanics and Engineering*, 196(21):2338–2357, 2007.
- [62] Francesco Riccardi, Ejona Kishta, and Benjamin Richard. A step-by-step global crack-tracking approach in e-fem simulations of quasi-brittle materials. *Engineering Fracture Mechanics*, 170:44 – 58, 2017. ISSN 0013-7944. doi: <https://doi.org/10.1016/j.engfracmech.2016.11.032>. URL <http://www.sciencedirect.com/science/article/pii/S0013794416306658>.
- [63] M A Crisfield. Snap-through and snap-back response in concrete structures and the dangers of under-integration. *International Journal for Numerical Methods in Engineering*, 22(3):751–767, 1986.
- [64] C Bosco and A Carpinteri. Discontinuous constitutive response of brittle matrix fibrous composites. *Journal of the Mechanics and Physics of Solids*, 43(2):261–274, 1995.
- [65] G Alfano and M A Crisfield. Finite element interface models for the delamination analysis of laminated composites: mechanical and computational issues. *International journal for numerical methods in engineering*, 50(7):1701–1736, 2001.